AFOSR-TR- 05-0730

LJI-R-85-318

②

LaJolla INSTITUTE

AD-A159 155

THEORETICAL STUDIES IN NONDESTRUCTIVE EVALUATION (NDE)[*]

Final Report
Contract Number F49620-81-0017

by

Bruce J. West
Center for Studies of Nonlinear Dynamics[†]
La Jolla Institute
3252 Holiday Court, Suite 208
La Jolla, CA 92037

DTIC FILE COPY

DTIC
SELECTED
SEP 1 0 1985
E

85 09 09 033

A159153

REPORT DOCUMENTATION PAGE	READ INSTRUCTIONS BEFORE COMPLETING FORM

1. REPORT NUMBER AFOSR-TR- 85-0730	2. GOVT ACCESSION NO.	3. RECIPIENT'S CATALOG NUMBER

4. TITLE (and Subtitle) THEORETICAL STUDIES IN NONDESTRUCTIVE EVALUATION	5. TYPE OF REPORT & PERIOD COVERED Final 01 JUL 80 to 14 FEB 84
	6. PERFORMING ORG. REPORT NUMBER
7. AUTHOR(s) Bruce J. West	8. CONTRACT OR GRANT NUMBER(s) F49620-81-K-0017
9. PERFORMING ORGANIZATION NAME AND ADDRESS La Jolla Institute 3252 Holiday Court, Suite 208 La Jolla CA 92037	10. PROGRAM ELEMENT, PROJECT, TASK AREA & WORK UNIT NUMBERS 61102F, 4285, A0 (DARPA)
11. CONTROLLING OFFICE NAME AND ADDRESS AFOSR/NE Bldg 410 Bolling AFB, DC 20332-6448	12. REPORT DATE April 1985
	13. NUMBER OF PAGES
14. MONITORING AGENCY NAME & ADDRESS(if different from Controlling Office) SAME	15. SECURITY CLASS. (of this report) UNCLASSIFIED
	15a. DECLASSIFICATION/DOWNGRADING SCHEDULE

16. DISTRIBUTION STATEMENT (of this Report)

Approved for public release; distribution unlimited.

17. DISTRIBUTION STATEMENT (of the abstract entered in Block 20, if different from Report)

18. SUPPLEMENTARY NOTES

19. KEY WORDS (Continue on reverse side if necessary and identify by block number)

Scattering Theory, The Fractal Dimension of Ultrasonic Scatterers.

20. ABSTRACT (Continue on reverse side if necessary and identify by block number)
See Attached

DD FORM 1 JAN 73 1473 EDITION OF 1 NOV 65 IS OBSOLETE

The technique developed by Montroll and West has been used to describe the discrete scattering of scalar waves from defects on a regular simple cubic lattice. The method makes no assumption about the symmetry of the scatterers and therefore can be applied to inhomogeneities of arbitrary shape. The only limitation of the technique is the maximum number of defects one can use to specify the scatterer, which in turn is determined by limitations in computation time.

The multiple scattering model proposed by Foldy and latter extended by Lax was implemented by West and Shlesinger as a means of evaluating the distribution of grains in polycrystalline materials.

If the material consists of grains such that the wavelength is much larger than the grain size then the density of scatterers probed by the acoustic wave is unchanged as the frequency is increased, provided that one remains in the Rayleigh scattering domain. If one is in the scattering domain where the wavelength is less than or equal to the grain size, then the density of scatterers increases no more rapidly than the square of the linear scale (a-squared) rather than as its cube as it would in the usual situation. This implies that the density of scatterers is a fractal in the stochastic scattering domain. Note also that the surface of a grain can have many scales and may in part be responsible for the fractal behavior observed in the phenomenological expression. Keywords:

FLD 19

1473 B

LJI-R-85-318

THEORETICAL STUDIES IN
NONDESTRUCTIVE EVALUATION (NDE)*

Final Report

Contract Number F49620-81-0017

by

Bruce J. West

Center for Studies of Nonlinear Dynamics†

La Jolla Institute

3252 Holiday Court, Suite 208

La Jolla, CA 92037

Accession For		
NTIS GRA&I		☒
DTIC TAB		☐
Unannounced		☐
Justification		
By		
Distribution/		
Availability Codes		
Dist	Avail and/or Special	
A-1		

DTIC
COPY
INSPECTED
3

TABLE OF CONTENTS

1. ACCOMPLISHMENTS UNDER FA 9620-81-0017

A. Scattering Theory

We proposed, under this contract, to apply a new analytic technique to the nondestructive evaluation (NDE) of materials. The technique had been developed by Montroll and West[1] to describe the discrete scattering of scalar waves from defects on a regular simple cubic lattice. The method makes no assumption about the symmetry of the scatterers and therefore can be applied to inhomogeneities of arbitrary shape. The majority of the approaches used in the past have had to either truncate the multiple scattering integrals at some appropriate order or restrict the investigation to scatterers having a high degree os symmetry. We, in LJI-R-83-229,[1] avoid both these limitations by characterizing a scatterer by a distribution of N defects and solving the scattering problem for these N defects *exactly*. The only limitation of the technique is the maximum number of defects one can use to specify the scatterer, which in turn is determined by limitations in computation time.

The problem posed by the scattering of a scalar wave from a fixed obstacle of known shape and composition is primarily numerical and involves the solution of a linear integral equation. The propagation of an ultrasonic wave through a homogeneous, isotropic elastic material is described by a scalar wave equation. The scattering of such a wave from an imperfection in the solid generates both longitudinal and transverse waves, which satisfy linear integral equations with a propagation kernel given by a Greens tensor. At present a numerically tractable theory for the scattering of an elastic wave from a flaw of arbitrary shape, i.e., one not possessing spatial symmetry, does not exist. In nondestructive evaluation (NDE), where such waves are used as probes to determine the shape, size and composition of flaws in materials, the analysis has been restricted to either long or short wave approximations. In the former case the Born approximation has been used extensively and in the latter a generalization of the diffractive geometric optics approximation originally due to Keller has been used.

In LJI-R-83-229 we limited our discussion to scalar waves scattering from inhomogeneities and examined properties of the scattered wavefield in the far field region. Among the scattering configurations we examined were line scatterers of finite length, i.e., hairline cracks, including the effects of ends in the crack and cracks of finite lateral extent also rectangular patches of scatterers. The exact scattered wavefield from such theoretically repelling,, but physically interesting objects has not been calculated previously.

We reviewed the mathematical formalism for the scattering of scalar waves from defects on a simple cubic lattice. The lattice was chosen for computational convenience and is not to be confused with the crystal lattice of the material. A real metal such as iron consists of an agglomeration of crystals having a characteristic dimension of 0.025 cm with arbitrary shapes and orientations. Each of these crystals is called a grain and there exists a distribution of grain sizes in such polycrystalline materials. The distribution of grain sizes determines the fracture micro-mechanics of the elastic material and can dominate such effects as crack formation and propagation as well as the attenuation of the ultrasonic waves. Under this contract we were not concerned with the generation or evolution of cracks, but rather with their detection. Thus we felt that the use of our computational lattice was justified for this preliminary investigation of S-wave scattering in NDE.[1] We showed that in the solution for the scattering of a wave from N defects no assumptions are made about the relative positioning of the defects. An extended scattering object is therefore represented by a distribution of N such defects. The Montroll-West model solution is not an exact representation of the scattering from a flaw, because the flaw is represented by only N defects. However, the ratio of determinant is the *exact* scattering solution to the N point representation of the flaw. The exact nature of the model enables one to exploit the method to determine the effects of interference and resonance in the specular reflection from cracks.

We also discussed the physical interpretation of the form of the solution to the N defect scattering problem. One can relate the terms in the expansion of the determinants to scattering diagrams and associate elements with particular multiple scattering effects. In this way various effects can be systematically suppressed by using approximations to the expanded form of the determinants. It was suggested that this technique can be used to check other approximation methods in situations where exact analytic or numerical calculations cannot be made using more standard methods.[1]

The extension of the above theory to the scattering of elastic waves in a material was made in LJI-R-82-174.[2] A spatially discrete lattice model of the scattering was developed and the discrete lattice Greens tensor that go over to the proper continuum form in the appropriate limit were constructed. The scattering from inhomogeneities on the lattice using these lattice Greens tensors enabled us to write the exact scattered wave field as the ratio of determinants. The elements of the determinants are all known quantities, i.e., they

are the strength of the inhomogeneities at the N scattering points. The formal scattered field from a single density discontinuity was evaluated in detail and shown to give for the components of the scattered wave displacement $\eta(l) = \eta^0(l) + \eta^s(l)$:

$$\eta_a^s(l) \simeq A_a(l_1) \frac{e^{ik_s l}}{|l|} + B_a(l_1) \frac{e^{ik_c l}}{|l|} .$$

The amplitude of the longitudinal (compression) components of the scattered wave are

$$A_a(l_1) \equiv \sum_\beta \frac{\delta\rho(l_1)}{4\pi\rho^0} k_s^2 (\delta_{a\beta} - \hat{l}_a \hat{l}_\beta) e^{-ik_c \cdot l_1} D_\beta(l_1)/\Delta_1$$

and the amplitudes of the transverse (shear) components of the scattered wave are

$$B_a(l_1) \equiv \sum_\beta \frac{\delta\rho(l_1)}{4\pi\rho^0} k_c^2 \hat{l}_a \hat{l}_\beta e^{-ik_c \cdot l_1} D_\beta(l_1)/\Delta_1 .$$

Here $\delta\rho(l_1)$ is the mass density change from the ambient value ρ^0 located at lattice point l_1; $\hat{l}_a$ is the unit vector in the a direction, k_s is the shear wave number determined by the shear speed V_s, i.e., $k_s = V_s/\omega$; k_c is the compression wave number and $D_\beta(l_1)$ is the scattering determinant[2] in the direction $\hat{k}_\beta$.

B. The Fractal Dimension of Ultrasonic Scatterers

Nondestructive methods, in particular the measurement of elastic waves, have become increasingly important in determining the microstructure of many materials in recent years. Material properties such as the distribution of grain sizes in polycrystalling materials, the degree of homogeneity, the existence of macroscopic cracks, inclusions, twin boundaries, dislocations, etc., all affect fracture micromechanisms and fracture control technology. The basis of the ultrasonic approach is the observation that the amplitude of low-frequency (long-wavelength) ultrasonic waves (of known amplitude and direction) are exponentially attenuated with distance, i.e. the wave intensity decays as $\exp[-\alpha(f)z]$, where z is the line-of-sight distance from the source and $\alpha(f)$ is a frequency dependent attenuation factor.

The standard theories of wave attenuation partition $\alpha(f)$ into two parts; the absorption attenuation coefficient $\alpha_a(f)$ and the scattering attenuation coefficient $\alpha_s(f)$. The absorption of energy from the ultrasonic wave arises from dislocation damping as well as magneto-elastic and thermo-elastic hysteresis and leads to the coefficient $\alpha_a(f) = Af$. The quantity A may itself be a function of frequency over a large frequency range depending on the material. The discontinuity in acoustic impedance occurring at grain boundaries and defect sites leads to elastic scattering. For a polycrystalling material of average grain size D an ultrasonic wave of wavelength λ and frequency f will have the scattering attenuation coefficient: for $\lambda \gg D$ (Rayleigh scattering domain) $\alpha_s(f) = S_1 D^3 f^4$, for $\lambda \le D$ (stochastic scattering domain) $\alpha_s(f) = S_2 D f^2$; and for $\lambda \ll D$ (diffusive domain $\alpha_s = S_3/D$) where S_1, S_2, and S_3 are related to the elastic moduli and the longitudinal and transverse sound speeds in a single crystal. Experimental data is fitted by these equation and the characteristic value of D is inferred.

In typical metals one encounters a range of grain sizes so that neither the Rayleigh nor stochastic scattering limits are appropriate. Instead both types of scattering are simultaneously present. In addition the absorption parameter A may be frequency dependent. Thus none of the above attenuation coefficients are used in practice, instead the phenomenological expression

$$\alpha(f) = Bf^\mu$$

has been adopted, where B and μ are frequency independent constants. It is expected, however, that variations in the microstructure of the material will lead to variations in B and μ, so that these parameters can be expressed in terms of certain structural properties of the material. We showed in LJI-R-84-276[3] that the parameter μ is a measure of the density of scatterers in the material.

In West and Shlesinger (1984)[4] we implemented the multiple scattering model proposed by Foldy and latter extended by Lax, wherein the wave number of a wave emerging from a region containing a density of scatterers ρ is

$$k^2 = k_0^2 + 4\pi\rho f(k) .$$

The function $f(k)$ is the forward scattering amplitude of a single scatter and is complex and k_0 is the incident wave number of the acoustic wave. In Reference

[4] we approximated the wave number k by the relation $k = k_0 + 2\rho f(k_0)/k_0 + i2\rho \text{Im} f(k_0)/k_0$. Then through the use of the optical theorem relating the total cross section of the scatterer to the imaginary part of the scattering amplitude, i.e., $\sigma_t \equiv 4\pi \text{Im} f(k_0)/k_0$, we obtained $k = k_0 + 2\rho \text{Re} f(k_0)/k_0 + i\rho\sigma_t/2\pi$. Thus the attenuation coefficient $\alpha(f) = 2\text{Im}(k)$, with $\bar{\sigma} \equiv \sigma_t/4\pi$ is

$$\alpha(f) = \rho\bar{\sigma}$$

indicating that the correlation among individual scatterers is negligible in this approximation. The scattering cross section, $\bar{\sigma}$ has the power-law frequency dependence f^s where $s = 0,2,4$ from the earlier theories of the frequency dependence of the attenuation coefficient.

To determine the total frequency dependence of $\alpha(f)$ we utilize the experimental observation that a high frequency elastic wave interacts with more scatterers than does a low frequency wave. Therefore the density of scatterers experienced by the incident wave is frequency dependent, i.e., $\rho = \rho(f)$. A wave of frequency f_1, will be scattered by $N_1(=\rho_1 V)$ defects (V is the volume of the sample and ρ_1, the density probed by the frequency f_1) and a wave of frequency f_2 will be scattered from N_2 defects. Thus if $f_2 < f_1$ then $\rho_2 < \rho_1$. For two real constants a and b we write

$$\rho(f_1) = b\rho(f_2) = b\rho(f_1/a) \text{ with } a,b, > 1$$

which has the scaling solution

$$\rho(f) = \text{const. } f^{\ln b/\ln a} \quad .$$

The exponent $\ln b/\ln a$ is reminiscent of a fractal dimension. Fractals are geometric objects having structure on an infinite number of scales. As an example consider a three dimensional distribution of mass points such that the quantity of mass $M(r)$ contained in a sphere of radius R increases with distance as $M(R)\alpha R^F$, $F \le 3$. The case $F = 3$ is the familiar situation for a uniform distribution of mass points. However, a self-similar distribution of mass points is described by a value of F less than three. In the usual case, when the mass is within a sphere of radius r and we have no information on scales below r, then the mass is assumed to have a uniform distribution. If we now examine the sphere on a finer scale, $r' = r/a$ say, we discover that what we had considered to be a single sphere to actually consist of b smaller sphere each of radius r/a.

If this process of increasing the resolution is continued ad *infinitum* we arrive at the expression (11) for the mass distribution of $F = \ln b / \ln a$. The quantity F is called the fractal dimension.[3,4]

The attenuation coefficient can now be written as $\alpha(f) = \rho(f)\bar{\sigma}(f) = Bf^\mu$ where B and μ are constants and μ is given by

$$\mu = s + \ln b \ln a \quad .$$

If the material consists of grains such that $\lambda \gg D$ then the density of scatterers probed by the acoustic wave is unchanged as the frequency is increased, provided that we remain in the Rayleigh scattering domain. In this case $B = 1$ so that $\mu = s = 4$. In practice the Rayleigh domain sets in at about $\lambda \sim 10D$. If we are in the scattering domain $\lambda \leq D$ then $S = 2$ in (11) and experimentally $\ln b / \ln a \leq 2$, i.e., $b \leq a^2$. Thus the density of scatterers increases no more rapidly than the square of the linear scale (a^2) rather than as its cube as it would in the usual situation. This result implies that the density of scatterers is a fractal in the stochastic scattering domain. Note also that the surface of a grain can have many scales and may in part be responsible for the fractal behavior observed in the phenomenological expression.

REFERENCES

1. "Scattering of Waves by Irregularities in Periodic Discrete Lattice Spaces II. Calculations," N. Pomphrey, E.W. Montroll and B.J. West, LJI R-83-229.

2. "Elastic Wave Scattering on a Lattice I. Informulation of an Exact Model," B.J. West, LJI-P. 92-175.

3. "Fractals in Scattering," B.J. West and M. Shlesinger, LJI-R-84-276.

4. "The Fractal Interpretation of the Weak Scattering of Elastic Waves," B.J. West and M.F. Shlesinger, J. Stat. Phys. **36**, 779 (1984).

2. WORKSHOP ON "QUANTITATIVE PREDICTIONS USING NDE"

We also proposed under this contract to bring together some of the top experimentalists and theoreticians in NDE to critique the state of the art in their respective specialties. This was done December 1 and 2, 1983 at the La Jolla Institute at a workshop on: "Quantitative Predictions Using NDE." The following are the abstracts of the talks presented at the workshop, in their order of presentation:

SUCCESSES AND FAILURES OF NUMERICAL METHODS FOR ELASTIC WAVE SCATTERING PROBLEMS

Vasundara V. Varadan

Ten years ago, with increased interest in NDE, came the realization that techniques available then for solving elastic wave scattering problems were woefully inadequate. Reliable results were not available even for spheres and cylinders, let alone for more interesting creatures like cracks. Several numerical methods were developed, as also asymptotic methods for the low- and high-frequency methods such as the Born Approximation. Numerical methods such as the T-matrix, MOOT and FEEM, BIE, etc., have been applied to several problems of interest in NDE with varying degrees of success. This talk will focus on the successes and failures of such methods as applied to NDE and future scope of such methods in the context of NDE.

SOME ULTRASONIC EXPERIMENTS IN MATERIALS CHARACTERIZATION

Laszlo Adler

Selected topics to cover recent experimental ultrasonic techniques to evaluate materials will be discussed. Problems to be addressed: scattering from inhomogeneities, in the bulk and outer surface, effect of anisotropy of the materials on wave propagation, and correlation between ultrasonic measurements and fracture mechanics.

NEW DEVELOPMENTS IN NONDESTRUCTIVE MEASUREMENTS OF BULK RESIDUAL STRESSES

Kamel Salama

Only in the case of surface stresses in components made of crystalline materials can nondestructive evaluation of stresses be performed by x-ray methods. Although considerably improved in the last decade, these methods still suffer from serious problems which severely restrict their applications.

Ultrasonic methods appear to hold the best promise in the nondestructive meas-
urements of bulk stresses in both crystalline and non-crystalline materials.
These methods are believed to utilize the anharmonic nature of the crystal lat-
tice, where the stress is directly related to the coefficients of higher-order
terms in the strain energy function. The exact mechanism in each of the
methods, however, has not yet been established.

In this presentation, new developments in ultrasonic methods to measure
residual stresses will be reviewed along with their limitations and potential appli-
cations. Also to be discussed, are some of the major theoretical advancements
which have been achieved in the last decade.

SPECULAR REFLECTION BY UNCOOPERATIVE CRACKS*

J. D. Achenbach

The failure processes that result in a crack generally produce rough crack
faces. Once crack opening has taken place, and the crack faces have undergone
the slightest relative sliding displacement, the crack will never completely close
again due to incompatibility of the rough crack faces. Under subsequent loading
conditions, the faces of the crack generally are not free of surface tractions, as
is assumed for a perfect mathematical crack, nor will there be perfect contact
between the crack faces. Unless the crack faces are completely separated, a
complicated interaction between the crack faces is to be expected, which will be
different for opening and closing of the crack on the one hand, and relative slid-
ing of the crack faces on the other.

The effects of interaction between contacting crack faces are of particular
interest in studies of crack detection and crack characterization by the use of
the specular reflection and scattering of ultrasonic waves. The idealized model
of a perfect mathematical crack acts as a perfect screen for reflection and
scattering. Scattering results for the perfect mathematical crack-model are
valid for a real crack if the amplitude of the incident wave is smaller than the
average crack-opening displacement prior to wave incidence, and if the
wavelength is much larger than a characteristic length of the roughness the
crack faces.

A crack with interacting crack faces may be a poor reflector, and thus
difficult to detect and to characterize. In this discussion, we investigate the loss
of specular reflection due to transmission across the crack faces by nonlinear
crack-face interactions. The crack is represented by a flaw plane of traction
continuity (the tractions may vanish) but possible displacement discontinuity.
The interaction between the crack faces is described by nonlinear relations
across the flaw plane between averaged tractions and averaged displacement
discontinuities and their derivatives.

The emphasis in the present paper is on cracks that are lightly closed, and
that may experience separation of the crack faces as well as further closure.
Since the resistance to crack closure is very different from the resistance to
crack opening, the problem is inherently nonlinear. If the crack should remain

closed at all times, a local perturbation about the closed state can be used to yield a linear problem statement. The postulated nonlinear flaw plane relations used in the present work contain a number of parameters which must be determined experimentally.

Time of preparation permitting, we will also present some preliminary results on reflection and transmission of incident waves by gratings of small cracks.

ANALYSIS OF MANY - DEFECT SYSTEMS

J. M. Richardson

In the general problem of quantitative NDE, the majority of past approaches are based upon the questionable assumption that the dominant defect or flaw (or at least a tractably small set of significant defects) has been identified before the beginning of the main body of the analysis. This concept, in its most simplistic form, is fundamental to most (but not all) treatments of probabilistic failure prediction and accept/reject optimization. Also, this concept, in a less simplistic form, underlies practically all signal processing approaches in the interpretation of ND measurements in the context of detection and flaw characterization. It is frequently assumed that a single significant, or partially significant, defect influences one (and only one) set of measurements. These oversimplifications and associated logical tangles are obviated by a more comprehensive approach to defect characterization and probabilistic failure prediction in which it is assumed in the pertinent stochastic models that the various significant types of defects occur in all possible numbers. It is convenient to use a specification of the many-defect state in terms of occupation numbers associated with small cells in single-defect state-space. Several approximate approaches to the analysis of such systems have been developed using methodologies derived from classical statistical mechanics. These results will be described with emphasis on limiting cases. The relation of these results to several crucial problems (e.g., retirement for cause, machining damage in ceramics, etc.) will be discussed.

ANALYSIS AND SYNTHESIS OF OPTIMIZED EDDY CURRENT PROBES*

B. A. Auld

The aim of this presentation is to give a coherent presentation of eddy current probe design, with emphasis on task-oriented choices of probe geometry. Flaw detection and sizing optimization will be discussed with respect to detection sensitivity and accuracy of inversion, taking probe geometry and operating frequency as design parameters. The theoretical base for these procedures will be presented, together with recent experimental comparisons of theory and experiment - including measurements of the probe field distributions and methods for utilizing these measurements in predicting probe performance.

ELASTIC WAVE INVERSE SCATTERING THEORY*

James H. Rose

The use of ultrasound to characterize flaws (size, shape, orientation and material properties) in structural materials is the topic of this talk. The problem of characterizing isolated flaws with sharp boundaries and simple shapes in a homogeneous, essentially isotropic background has been systematically addressed over the last several years. Theoretical inverse scattering methods have been proposed based on the long wavelength, the short wavelength and the weak scattering limit (the inverse Born approximation). These theories have been tested experimentally and good agreement has been obtained. A brief summary of these developments and their physical bases will be given.

Then the talk will turn to the problem of characterizing flaws in parts with complex geometries and flaws which lie near surfaces. Here the recent experiments of Hsu et al. (1) and the measurement model of Thompson and Gray (2) will be emphasized.

Finally, various unsolved problems will be introduced and the possible direction of future work in the field will be discussed. Solutions are needed for more complicated flaws in a simple medium. For example, the characterization of multiple flaws (porosity) is an outstanding problem as is the characterization of complicated, bifurcated cracks. Secondly, the characterization of simple flaws in complicated media is needed (e.g., delaminations in composite structure). Finally, a brief mention will be made of the need to develop a suitable inverse scattering theory for ultrasonic surface waves.

1. D.K. Hsu, J.H. Rose and D.O. Thompson, J. Nondestructive Evaluation, in press.

2. R.B. Thompson and T.A. Gray, JASA **74**, 1279 (1983).

APPENDIX

Talks presented at the Workshop on: *Quantitative Predictions Using NDE* held at the La Jolla Institute, December 1-2, 1983.

SOME ULTRASONIC EXPERIMENTS
IN MATERIAL CHARACTERIZATION

Laszlo Adler
Department of Welding Engineering
The Ohio State University
Columbus, OH 43210

INTRODUCTION

Recent developments of materials characterization by ultrasonic waves is summarized by presenting a systematic approach to discontinuity analysis. Fig. 1 presents a systematic approach to ultrasonic evaluation of material structures which may be a weld or a joint, for example:

- Locate all flaws
- Characterize each flaw (determine size, shape, orientation and composition)
- Characterize the material (determine the elastic properties, grain size, surface roughness, etc.)
- Evaluate the seriousness of the flaws' presence (using fracture mechanics techniques).

In order to determine the presence (or absence) or weld discontinuities, an ultrasonic image is produced. Defects will be delineated as areas of increased ultrasonic-echo return. For flaws large compared with the beam dimensions, the ultrasonic image shows the extent of the defect. Flaws on the order of and smaller than the ultrasonic wavelength scatter the incident sound beam. Some of this energy returns to the transducer and appears on the image as a weakly scattering region in the material. Regions such as these are flagged for later investigation.

Next, the characteristics of the weld metal are measured. The grain structure and roughness of the ultrasonic beam entrance surface will have an effect on all subsequent measurements, and so must be determined. In addition, the mechanical properties of the material surrounding any flaws will profoundly affect the strength of the weld. Also, regions of the weld containing dense porosity or clouds of inclusions will lower weld strength. Determinations of the concentration and size distribution of voids or inclusions should permit calculations of estimated weld mechanical properties.

One now returns to the suspect regions in the welded structure, namely areas of increased echo return in the ultrasonic image. A broadband ultrasonic wave is directed toward the suspect region and the backscattered signal is then processed to obtain a magnitude spectrum (amplitude versus frequency). If the spectrum shows deep and periodic modulation, the suspect region contains a planar discontinuity (e.g. crack). If, however, the spectrum is relatively smooth, the flaw is volumetric (e.g. pore). Characterization of the defect requires further signal processing. Discrimination of planar from volumetric discontinuities permits the appropriate processing algorithm to be selected.

Ultrasonic spectroscopy (using cepstral analysis) is utilized for determining the size of crack-like flaws. Upon processing, the distance (along the ultrasonic beam path) is calculated which separates the near and far edges of the flaw. Interrogation of the defect from a number of angles may be used to obtain the flaw's size and shape.

Volumetric defects are characterized by "Born inversion" processing. This algorithm returns both a line-of-sight estimate of flaw radius and the cross-sectional area of the flaw (along the ultrasonic beam path). "Observation" of the defect at a number of "look angles" discloses its shape and dimensions.

Once all flaws are characterized, data tabulating:
- Coordinates of all flaws
- Shape and size of all defects
- Material elastic properties (Young's and shear moduli, Poisson's ratio)
- RMS surface roughness
- Concentration and size distribution for areas containing clouds, of porosity, or inclusions

can be output for evaluation using fracture mechanics techniques.
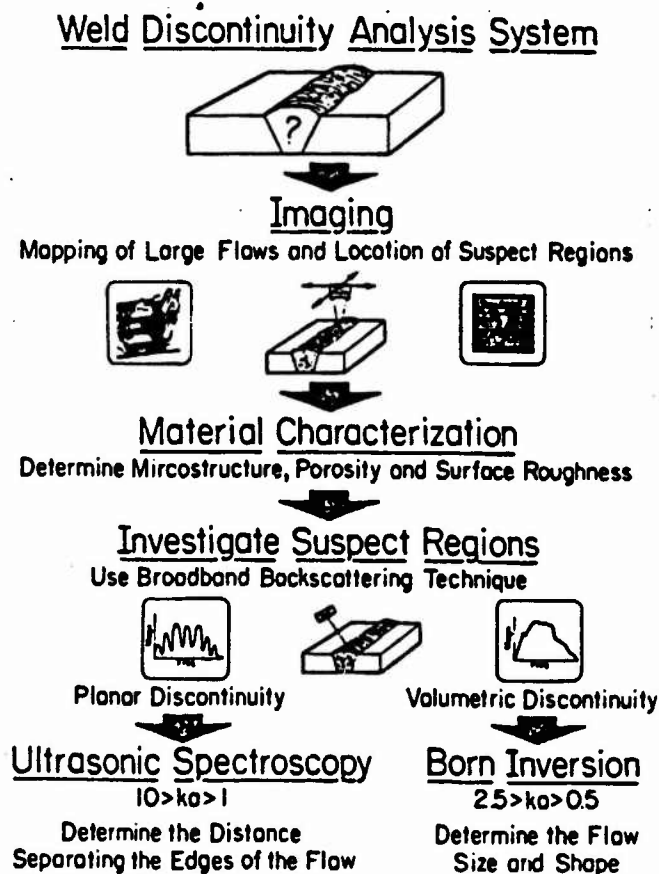

Weld Discontinuity Analysis System

Imaging
Mapping of Large Flaws and Location of Suspect Regions

Material Characterization
Determine Mircostructure, Porosity and Surface Roughness

Investigate Suspect Regions
Use Broadband Backscattering Technique

Planor Discontinuity   Volumetric Discontinuity

Ultrasonic Spectroscopy
$10 > ka > 1$
Determine the Distance
Separating the Edges of the Flow

Born Inversion
$2.5 > ka > 0.5$
Determine the Flow
Size and Shape

Fig. 1. Systematic Procedure for Ultrasonic Nondestructive Evaluation

DESCRIPTION OF SYSTEM ELEMENTS

IMAGING

The purpose of ultrasonic imaging is to locate regions in the weld which contain flaws. A focused ultrasonic beam is directed toward the weld. Changes in material elastic properties or density will cause reflection and scattering of the incident beam. A portion of this echo energy is intercepted by the receiving transducer. The receiver output is recorded with the spatial coordinates of the scattering region (Fig. 2). If the entire volume of the weld is scanned one builds up a 3-dimensional map of echo amplitude versus position.
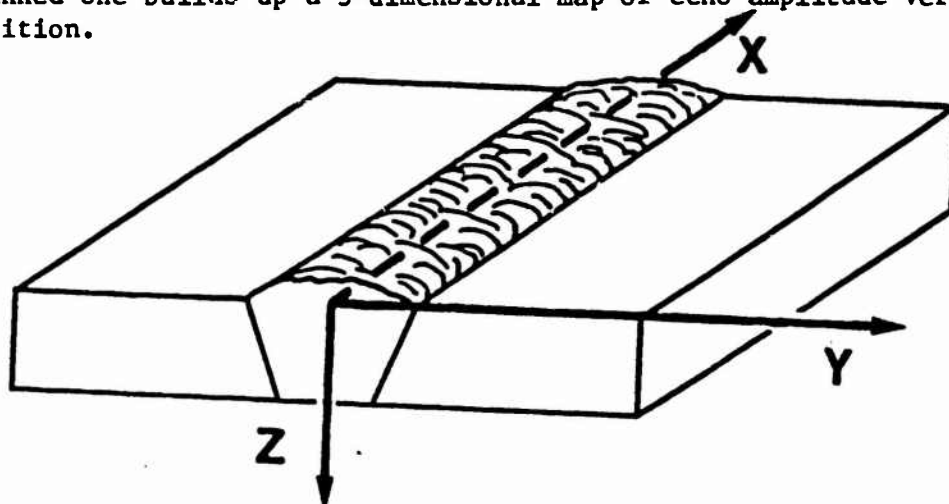
Fig. 2. Assignment of Coordinates to a Weld.

Display Modes

Display of echo information is normally presented one plane at a time. The image is termed a C-scan (echo amplitude at constant depth) if the image plane is parallel to the sample surface (x-y plane). It is a B-scan (display brightness indicates echo amplitude) if any other plane (e.g. x-z, y-z or oblique) is presented. It is also possible to display the echo strength as a brightness-modulated three-dimensional isometric presentation (Fig. 3). Echo amplitude is shown as display height as a function of two orthogonal spatial coordinates. Because of the ease in implementing this isometric display format, it was chosen for all our B- and C-scans.

Image Optimization

The scattering amplitude measured for a particular element in the weld is dependent on
- the ultrasonic wave mode (longitudinal, shear, surface wave)
- the frequency of the incident wave
- the incident angle, and
- the spatial distribution of the incident beam.

Each of these factors may be adjusted such that flaw detectibility is optimized. Analytical, as well as, experimental work is needed in this area.
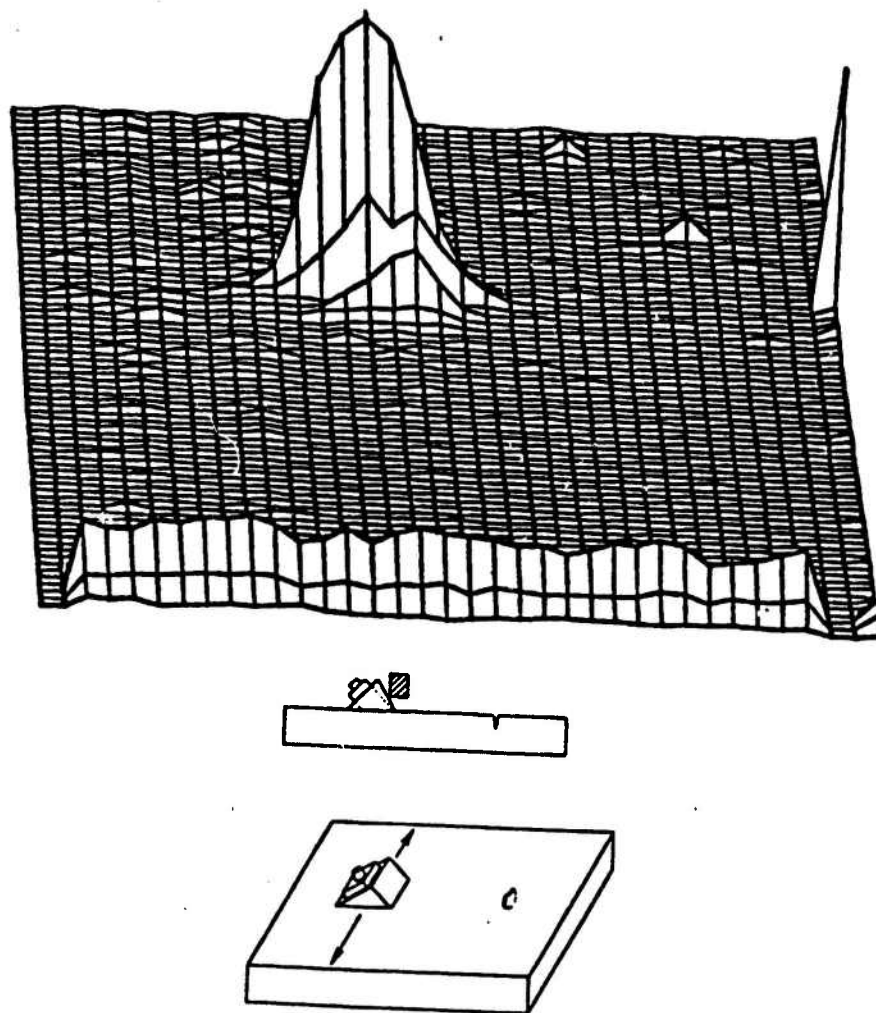
Fig. 3. B-Scan Ultrasonic Image of a Fatigue Crack (a). The Rayleigh surface waves used (b) to investigate the crack were generated by the wedge method.

Image Processing

It is possible to accentuate the presence of flaws in an ultrasonic image by postprocessing. A method, gradient processing, for enhancing edges in an image is introduced here. Let the echo amplitude as a function of spatial position be represented by $f(x,z)$ [B-scan display mode]. Then the gradient is defined as the vector[1]

$$G[f(x,z)] = \begin{bmatrix} \dfrac{\delta f}{\delta x} \\[2ex] \dfrac{\delta f}{\delta z} \end{bmatrix} . \tag{1}$$

The gradient vector points in the direction of the maximum rate of change of $f(x,z)$ and its magnitude gives the maximum rate of change in $f(x,z)$ per unit distance in the direction of G. For manipulation of the digital image, the magnitude of the gradient is approximated by

$$G[f(x,z)] = |f(x,z) - f(x+1,z)| + |f(x,z) - f(x,z+1)| . \tag{2}$$

The gradient of the ultrasonic image is displayed if the gradient is above a threshold value. If the gradient is below threshold (presumably the case for pixels representing unflawed regions in the weld) the image pixel is set to zero. Flaws in the processed image stand out more clearly (Fig. 4b) than in the original ultrasonic image (Fig. 4a). Research is needed for adaptive threshold setting, other methods of image processing and automated flaw recognition schemes.
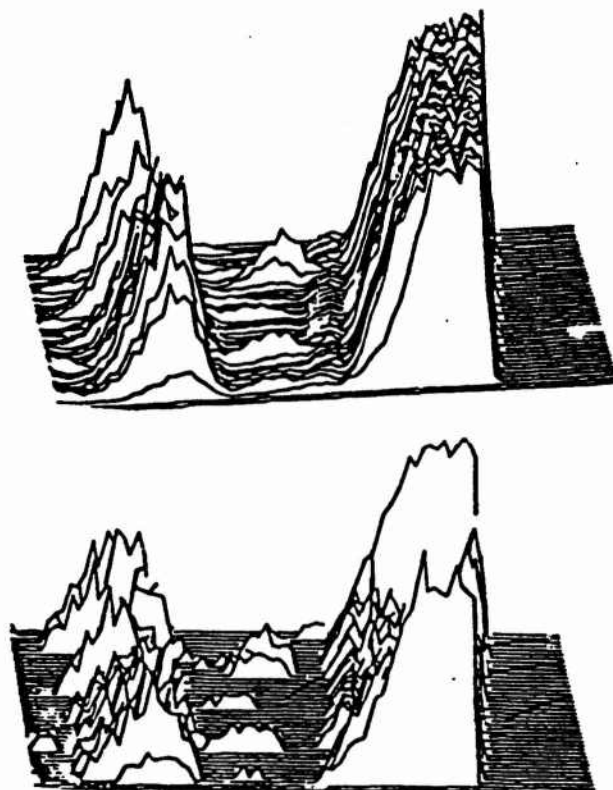

Fig. 4 Ultrasonic B-Scan Images of a Specimen containing Multiple Defects. Image before (a) and after (b) gradient processing.

MATERIALS CHARACTERIZATION

The mechanical properties of the material in which a flaw is embedded may be as important as defect size in determining strength. Material characteristics which are of importance are listed in Table I. It is possible to nondestructively determine many of these properties from ultrasonic velocity and attenuation measurements. Both analytical and experimental studies have been made to determine how frequency-dependent velocity and attenuation measurements may be used to infer the concentration and size of pores occurring in dense clouds.

Inhomogeneities (such as pores and inclusions) weaken the structural components in which they occur. It is important to nondestructively determine the size distribution and concentration of pores or inclusions. A multiple scattering theory was developed for treating wave propagation through inhomogeneous material; Matrix and second phase elastic properties inclusion concentration and size distribution are used as input. Dispersion and frequency-dependent attenuation are calculated using theory.

Table 1

MATERIAL PROPERTIES

Tensile Modulus
Shear Modulus
Tensile Strength
Shear Strength
Bond Strength
Hardness
Surface Finish
Impace Strength
Fracture Toughness
Anisotropy
Microstructure
Grain Size
Porosity, Void Concentration
Phase Composition
Hardening Depth
Residual Stress
Heat Treatment Profile
Fatigue Damage

Ultrasonic Wave Propagation in Cast Iron-Graphite Composite

The same multiple scattering treatment applied to porous media may also be used to analyze the problem of an ultrasonic wave traversing a material containing clouds of solid inclusions. Cast iron containing compact flake and nodular graphite, and also specimens of gray iron is studied. Because the graphite in nodular iron appears mostly as spheres, it was thought the multiple scattering theory could be used with only minor changes to include the elastic properties of the graphite nodules.

The properties of the cast iron matrix were estimated from ultrasonic velocity measurements on a sample of 1045 steel. This type of steel was chosen because it has approximately the same relative

percentages of ferrite and pearlite. Table II lists pertinent material properties for the matrix (iron) and inclusions (graphite nodules). Elastic moduli were calculated from the velocities.

Table II. Properties of the Constituents in Nodular Cast Iron.

Velocities (km/sec)

Material	Longitudinal	Transverse	Density (g/cm^3)
iron (1045 steel)	5.8	3.1	7.2
graphite	3.2	1.8	2.2

Values for the matrix material, iron, and the inclusions, graphite spheres were input to the multiple scattering theory to determine the phase velocity and attenuation as a function of frequency. Narrow-band and broadband ultrasonic experiments were performed on carefully prepared specimens of cast iron. Fig. 5 plots theoretically-determined attenuation and experimental measurements. The shape of the curves are identical; however, there is an offset. We ascribe this to incorrect assumptions of the wave speed in the graphite and to the fact we assumed a uniform size of graphite nodules, when there is actually a distribution of sizes.

Surface Roughness

The condition of the surface through which ultrasonic beam enters the material can have a profound effect on the frequency content of the pulse, the angle of the refracted energy and on the spatial distribution of the beam in the solid. Both imaging and defect characterization techniques will be affected by the surface finish on the weld under evaluation. Much of the unreliability of contact ultrasonic testing arises from multipath effects and trapped air due to roughness on the sample surface.

We have begun studies aimed at nondestructively inferring parameters describing surface roughness (rms roughness and correlation length for randomly-rough surfaces and periodicity and peak to valley height for periodic surfaces). Surface roughness may be measured ultrasonically from the angular or frequency dependence of wave scattering.

Ultrasonic measurement of rms roughness (h) may be carried out in the following manner. An ultrasonic transducer, operated in the pulse-echo mode, is used to record the intensity <I> of backscattered ultrasonic compressional waves. The experiment is repeated for a smooth-surfaced sample of the same material (giving I_0).

If low frequencies are used, the backscattered intensity is approximated as

$$<I> = I_0 e^{-k^2 h^2}. \tag{3}$$

where k is the wave number of the ultrasound in the liquid bath. The roughness, h, may be estimated from

$$h \sim \left(\frac{\Delta dB}{-17.37 k^2} \right)^{\frac{1}{2}} \tag{4}$$

where ΔdB is the relative amplitude of the waves backscattered from the rough surface compared to that of the smooth surface. The advantages of the ultrasonic measurement of surface roughness are

- it is nondestructive
- determinations may be made rapidly
- whereas mechanical profilometers measure roughness only along the line of stylus traverse, the ultrasonic method averages over the entire insonified area (be it small or large).
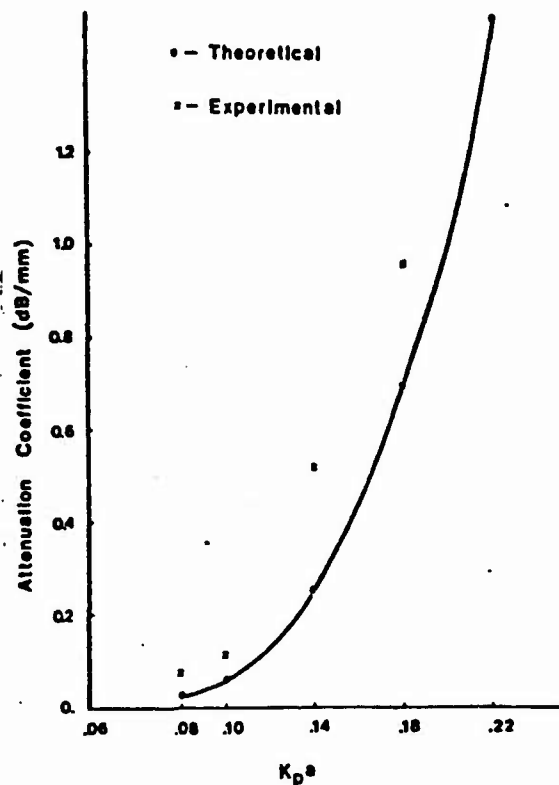

Fig. 5. Attenuation of Ultrasonic Waves in Nodular Cast Iron as a Function of Frequency (o - multiple scattering theory and x - experimental).

DEFECT CHARACTERIZATION

Ultrasonic images produced in the first stage of our evaluation disclosed the extent of large flaws and identified weakly scattering regions as areas potentially containing smaller defects. For a fracture mechanics evaluation, the size and shape of these small discontinuities is required (in addition to their location, as determined from the ultrasonic image). Flaw characteristics may be determined from ultrasonic scattering data; however, the defect must first be classified as volumetric (3-dimensional, e.g. pore or inclusion) or planar (2-dimensional, e.g. crack-like).

The classification of defect type is carried out by identifying discriminatory features in the backscattering frequency spectrum. The procedure below is followed.

1) A broadband ultrasonic pulse is directed toward the suspect region in the weld.
2) The backscattered signal from the region is sampled, digitized and stored in computer memory.
3) A system normalization signal is acquired by sending the incident pulse through an unflawed region in the material toward a perfect reflector (polished solid-air surface).
4) Perturbing effects of the data acquisition system and material intervening between the ultrasonic transducer and the defect are removed by deconvolving the defect signal by the signal from the reference reflector.
5) The magnitude spectrum is displayed.
   - The defect is classified as planar if the spectrum has deep, periodic modulation (explanation given later).
   - The defect is classified as a volumetric flaw if the spectrum is relatively smooth.
6) If there is some ambiguity in classifying the defect type (5), then the suspect region is interrogated from a number of angles.
   - A planar discontinuity will return large backscattering signals for orientations in which the incident ultrasonic beam is directed normal to the plane of the flaw.
   - Amplitude of signals returned from a volumetric discontinuity depend less strongly on angle.
7) If the discontinuity is planar, an inversion scheme termed ultrasonic spectroscopy is followed.
8) If a volumetric flaw is to be characterized, the Born inversion algorithm is utilized.

The Born inversion procedure is summarized here.

Born Inversion

As an ultrasonic wave strikes a volumetric flaw (Fig. 6), the cross-sectional area encountered increases as the wave propagates. When the wave is just incident on the defect (time, t_1) the area encountered is minimal. As the wave moves onward (time t_2, then t_3, . . .) they are encountered increases (A_2, A_3, . . .). The cross-sectional of the flaw reaches a maximum when the wavefront reaches the center of the flaw. The area encountered decreases thereafter. The Born inversion algorithm returns the area function A_i versus t_i.

From this, a line-of-sight estimate of flaw radius may be calculated.

Ultrasonic Spectroscopy

Ultrasonic spectroscopy applied to defect characterization was pioneered by Adler, et. al.[1,2,3] The fundamental ideas underlying the technique are summarized here (details may be found in the book by Fitting and Adler,[4]).
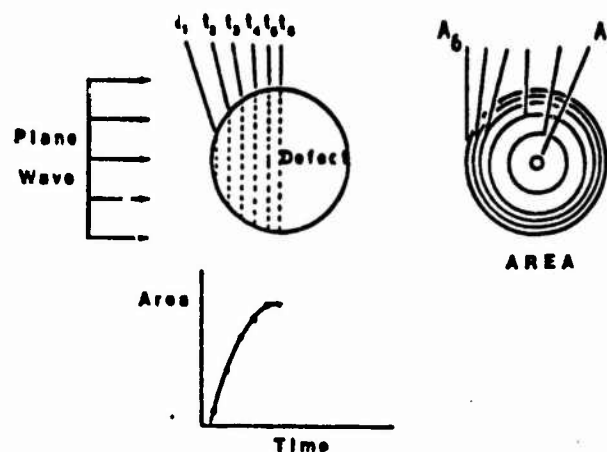
Fig. 6. Plane Wave Encountering a Scatterer.
        a) Position of wavefront at times t_i.
        b) Area of the scatterer encountered at times t_i, and
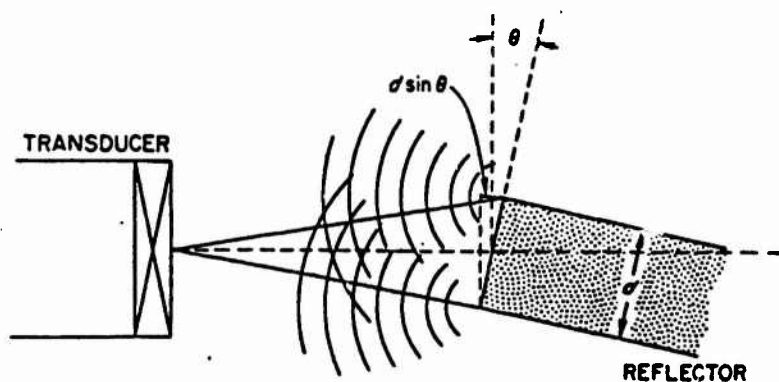   c) Area function.

Fig. 7. Ultrasonic Waves Scattered from the Edges of a Planar Reflector.

An ultrasonic wave directed toward a planar discontinuity will be in part specularly reflected from it, but also scattering will occur from the near and far edges (flashpoints, [5]) of the flaw (Fig. 7). If the echo is transformed to the frequency domain (via the Fast Fourier Transform, FFT) the time spacing of the signals may be determined.

Consider a single signal $y(t)$ which has a spectrum $Y(2\pi f)$. The magnitude spectrum of two such signals, separated in time by $2t_o$, has been shown [6] to be $|2 \cos 2\pi f\, t_o||Y(2\pi f)|$. That is the spectrum is

modulated, and the period is determined by the time separation (Fig. 8). Th' spacing (Δf) of the frequency minima may be used to determine the time separation (Δt) of the ultrasonic echoes:

$$\Delta f = 1/2t_0 = 1/\Delta t. \tag{5}$$

If the wave speed is known, then the separation of the near and far flaw edges may be calculated and the flaw dimensions determined from

$$d = \frac{c}{2 \Delta f \sin\theta} . \tag{6}$$

The orientation of the crack (θ) may be determined from a number of angular measurements.

EXAMPLES OF ULTRASONIC NONDESTRUCTIVE WELD EVALUATION

As a test of our systematic method for evaluating welded structures (Fig. 1 and previous descriptions) we began with two welds containing well-characterized defects.

Weld sample #2 was carefully prepared to contain only planar discontinuities. Three artificial flaws, nominally 1/16", 1'8" and 1'4" in diameter were incorporated into the weld, along its center line (Fig. 8). T' e plane of the defects was parallel to the sample surface. Both the top and bottom surfaces of the specimen were ground flat.
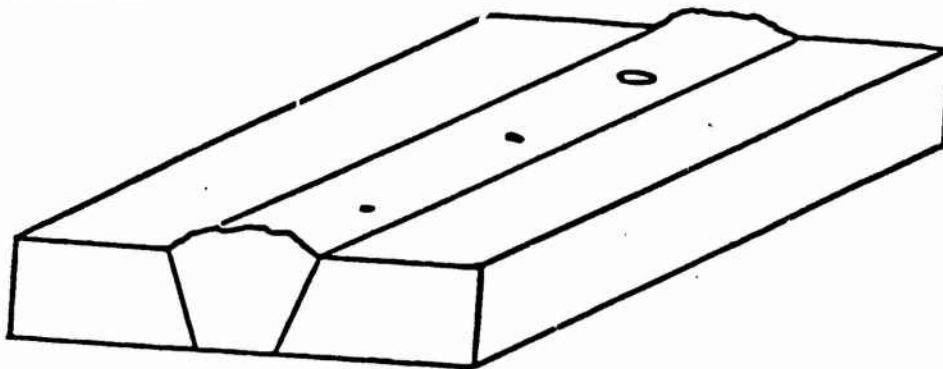

Fig. 8. Weld Sample #2 Containing Planar Discontinuities 1/16", 1/8" and 1/4" in Diameter.

IMAGING

A 5 MHz focused transducer (approximately 6" focal distance, 1" diameter) was scanned in a water bath above the weld. The water bath length was adjusted to focus the ultrasonic beam approximately at the depth the discontinuities were thought to occur. Spacing between transducer positions (along the weld) was 5 mm.

- the ultrasonic waveform returning from the weld is sampled, digitized and displayed (Fig. 8).
- the signal is full-wave rectified (Fig. 8).
- an estimate of the envelope of the waveform is determined

(Fig. 8).

* the number of positions along the weld where the transducer will be located is input (Fig. 9).
* wave speed for the mode of ultrasound used in the imaging is input (Fig. 9).
* the depth increment at which the echo amplitude is to be sampled is input (Fig. 9).
* a file name identifying the image data to be stored is given (Fig. 9) and
* the depth (time) range to be used for image display is defined (using the graphic terminal's cursor) (indicated by the vertical lines in Fig. 10).
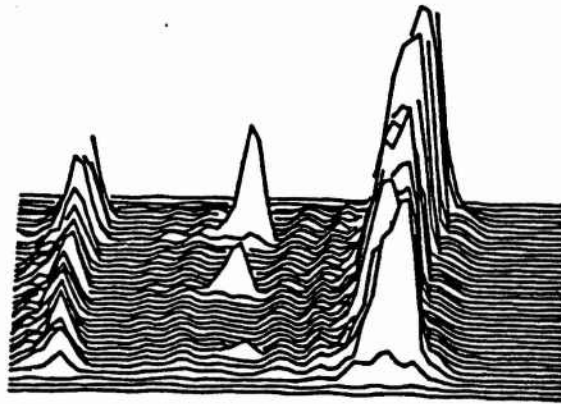

Fig. 9.   B-Scan Ultrasonic Image of a Weld Containing Three Planar Discontinuities (1/16", 1/8" and 1/4" in Diameter).
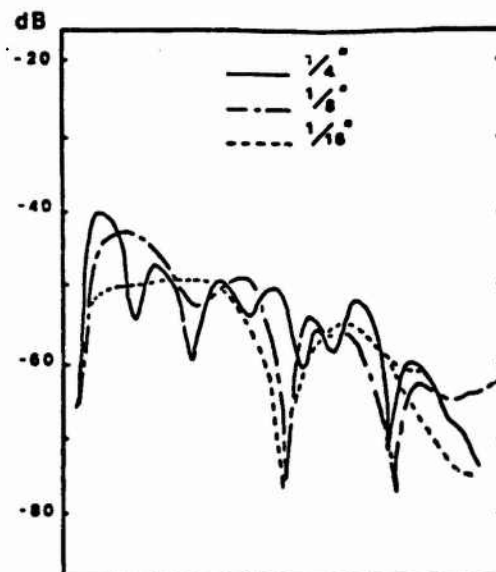

Fig. 10.   Backscattering Spectra from Suspect Regions in Weld #2.

Ultrasonic Spectroscopy

Broadband ultrasonic pulses from the 15 MHz unfocused transducer were coupled to the weld through a 6" water path. Backscattering signals were acquired for each flaw at 0-, 10- and 20-degree refracted angles in the solid. The spectra computed from these signals was plotted versus frequency. The absence of deep modulation at 0-degrees indicates the plane of each flaw is approximately parallel to the surface of the weld. The average spacing of minima in the spectra was determined (Table III) and equation (6) used to calculate the flaw diameter.

Table III. Average Spacing of Minima in the Backscattering Spectra from Flaws in Weld #2.

ID	10-degree Measurement	20-degree Measurement
A	9 MHz	4 MHz
B	4.7 MHz	2.3 MHz
C	2.55 MHz	1.13 MHz

Nondestructive Evaluation Summary for Weld #2

Longitudinal Wave Speed: 5939 m/sec

Shear Wave Speed: 3627 m/sec

Young's Modulus: 2.566

Shear Modulus: 8.219×10^{10}

Poisson's Ratio: 0.283

Suspect Regions:

ID	X	Y	Z
A	2.0 cm	0	7.5
B	7.5 cm	0	7.5
C	12.5 cm	0	7.5

Flaw Type:

ID	Type
A	planar
B	planar
C	planar

Flaw Orientation:

ID	Angle with Respect to Surface
A	0°
B	0°
C	0°

Flaw Dimension:
(assume circularly symmetric)

ID	10° Measurement	20° Measurement
A	1.8mm	2.06 mm
B	3.5 mm	3.6 mm
C	6.36 mm	7.3 mm

Compare these ultrasonically determined results with the actual position and dimensions below:

ID	X	Y	Z	Diameter (mm)
A	1.8cm	0	7.5cm	1.6 mm
B	7 cm	0	8cm	3.2 mm
C	12.05cm	0	8cm	6.35 mm

REFERENCES

1. H. L. Whaley and L. Adler, "Flaw Characterization by Ultrasonic Frequency Analysis", <u>Mat. Eval.</u>, <u>29</u> (8), (1971).
2. H. L. Whaley and L. Adler, "Model for the Determination of the Size and Orientation of Reflectors from Ultrasonic Frequency Analysis", <u>J. Acoust. Soc. Am.</u>, <u>48</u> (1), (1970).
3. H. L. Whaley and L. Adler, "A New Technique for Ultrasonic Flaw Determination by Spectral Analysis," Technical Memo, Oak Ridge National Laboratory, ORNL-TM-3056, (1970).
4. D. W. Fitting and L. Adler, <u>Ultrasonic Spectral Analysis for Nondestructive Evaluation</u>, Plenum Press, New York (1981).
5. J. D. Achenbach, L. Adler, D. K. Lewis and H. McMaken, "Diffraction of Ultrasonic Waves by Penny-Shaped Cracks in Metals: Theory and Experiment", <u>J. Acoust. Soc. Am.</u>, <u>66</u> (6), (1979).
6. W. A. Simpson, "A Fourier Model for Ultrasonic Frequency Analysis", <u>Mat. Eval.</u>, <u>34</u> (12), (1976).

ULTRASONIC SCATTERING PROBLEMS WITH APPLICATIONS TO QNDE

J. D. Achenbach
Northwestern University, Evanston, IL. 60201

Y. C. Angel
Rice University, Houston, TX. 77001

ABSTRACT

A useful non-destructive method for flaw characterization is
based on scattering of ultrasonic waves. This paper is concerned
with scattering by cracks. An exact formulation of the direct
problem, which leads to numerical results for the scattered field
in the frequency domain, is briefly reviewed. A very useful
approximate analytical approach is based on elastodynamic ray
theory. For crack-like flaws, the high-frequency scattered signal
outside of the zone of specular reflection is primarily generated
by edge diffraction at "flash points" on the crack edge. For the
inverse problem, crack mapping methods have been developed which
are based on inverse ray tracing. Deviations from perfect
"mathematical" crack geometries and isotropic material behavior may
significantly affect the scattered field. Nonlinear crack-face
interactions and reflection by partially closed flaw planes are
briefly discussed. Scattered-field results for an isotropic and a
transversely isotropic solid are compared.

1. INTRODUCTION

Failure of structural components is often initiated by the
presence of flaws which are inherent in the bulk material, or
which appear either in the course of the manufacturing process or
after a period of service. In a damage-tolerant design philosophy,
flaws are acceptable if they are sufficiently small so that they
will not lead to failure during the service life of the structure.
As part of a damage-tolerant design philosophy it is important to
have reliable methods of quantitative non-destructive evaluation
(QNDE), not only to detect the presence and the approximate
location of a flaw, but also to determine its size, shape, and
orientation.

One of the most useful QNDE methods is based on the scattering
of elastic (ultrasonic) waves by flaws in solids. The scattered-
field approach attempts to infer geometrical characteristics of a
flaw from either the angular dependence of its far-field
scattering amplitude at fixed frequency, or from the frequency
dependence of its far-field scattering amplitude at fixed angles.

In experimental work on quantitative flaw definition by the

ultrasonic pulse method, either the pulse-echo method with one
transducer or the pitch-catch method with two transducers is used.
The transducer(s) may be either in direct contact with the specimen,
or transducer(s) and specimen may be immersed in a water bath.
Most experimental setups include instrumentation to gate out and
spectrum analyze the signal diffracted by a flaw. The raw
scattering data generally need to be corrected for transducer trans-
fer functions and other characteristics of the system, which have
been obtained on the basis of appropriate calibrations. After
processing, amplitudes and phase functions are available as
functions of the frequency and the scattering angle. These experi-
mental data can then be directly compared with theoretical results.

The solution to the direct scattering problem, that is, the
computation of the field generated when an ultrasonic wave is
scattered by a known flaw, is a necessary preliminary to the
solution of the inverse problem, which is the problem of inferring
the geometrical characteristics of an unknown flaw from either the
angular dependence of the amplitude of the scattered far-field at
fixed frequency, or from the frequency dependence of the far-field
amplitude at fixed angle. In recent years analytical methods have
been developed to investigate scattering of elastic waves by
interior cracks as well as by surface-breaking cracks, in both the
high- and the low-frequency domains.

2. DIRECT PROBLEM - INTEGRAL EQUATION APPROACH

Scattering of time-harmonic signals by cracks has been
analyzed extensively on the basis of linearized elasticity theory
for a homogeneous, isotropic solid. The propagation of waves in
such solids is a classical area of investigation. The equations
governing elastodynamic theory, and several pertinent mathematical
techniques to obtain solutions, have been discussed in detail
elsewhere[1].

From the theoretical point of view a flat crack is a planar
surface across which the displacement can be discontinuous. The
exact mathematical formulation of the elastodynamic field generated
by the presence of a crack is rather complicated if the displace-
ment discontinuities are not known a-priori, as is the case for
scattering problems. Scattering of an incident wave by a crack is
a mixed boundary value problem, whose exact solution satisfies
one or more (generally singular) integral equations for the dis-
placement discontinuities. Only for a semi-infinite crack can an
analytical solution conveniently be obtained. The solution of the
system of integral equations for a crack of finite dimensions
requires a substantial amount of numerical analysis.

Let u_i^{in} define the components of the incident displacement
field for the crack scattering problem. In the usual manner the

scattered field u_i^{sc} is defined as the total field, u_i^{tot}, minus the incident field, i.e., $u_i^{tot} = u_i^{in} + u_i^{sc}$. The components of the corresponding stress tensors are τ_{ij}^{tot}, τ_{ij}^{in}, and τ_{ij}^{sc}. Usually the crack is assumed to be free of surface tractions; the conditions on the crack faces A^+ and A^- then are

$$\text{on } A^+ \text{ and } A^-: \quad \tau_{ij}^{sc} n_j = - \tau_{ij}^{in} n_j \; , \tag{2.1}$$

where n_j are the components of the normals to the crack faces. For a flat crack the scattered field may be expressed in the form[2]

$$u_k^{sc}(\underset{\sim}{x}) = - \int_{A^+} \tau_{ij;k}^{G}(\underset{\sim}{x}-\underset{\sim}{X}) \, [u_i^{sc}(\underset{\sim}{X})] n_j^+ dA(\underset{\sim}{X}) \; , \tag{2.2}$$

where n^+ is directed from A^- to A^+, $\tau_{ij;k}^{G}$ is the Green's stress tensor, and $[u^{sc}(\underset{\sim}{X})] = u^{sc}(\underset{\sim}{X}+\underset{\sim}{0}) - u^{sc}(\underset{\sim}{X}-\underset{\sim}{0})$, is the crack-opening displacement. Here $\underset{\sim}{X} \pm \underset{\sim}{0}$ correspond to the faces A^+ and A^-, respectively. Equation (2.2) gives an exact representation. The stresses according to (2.2) can be obtained by substitution into Hooke's law. Then by letting $\underset{\sim}{x}$ approach A^+, the stresses should satisfy (2.1). The resulting equations are integral equations for $[u_i^{sc}]$. These equations require careful handling, because the integrands contain singularities.

For simple geometries, such as penny-shaped cracks and two-dimensional slits, it is convenient to use Fourier transform techniques to derive a governing system of dual integral equations. These kinds of equations can be reduced to a single singular integral equation, which can then be solved numerically.[2]

The integral equation approach has been used to obtain solutions for scattering by surface-breaking and sub-surface cracks. Analytical, numerical, and experimental results have been reviewed by Achenbach et al[3]. For a surface-breaking crack, theoretical and experimental results have been compared for the case of normal incidence. Figure 1 shows a comparison between theoretical and experimental transmission coefficients obtained by Yew et al[4]. Experimental results for reflection of a surface wave by a sub-surface crack oriented normal to the free surface were obtained by Khuri-Yakub et al[5]. Figures 2 and 3 show theoretical and experimental results for the reflection coefficient.

In two well-known approximate theories, which are valid at low and high frequencies, respectively, a form of $[u^{sc}(\underset{\sim}{X})]$ is
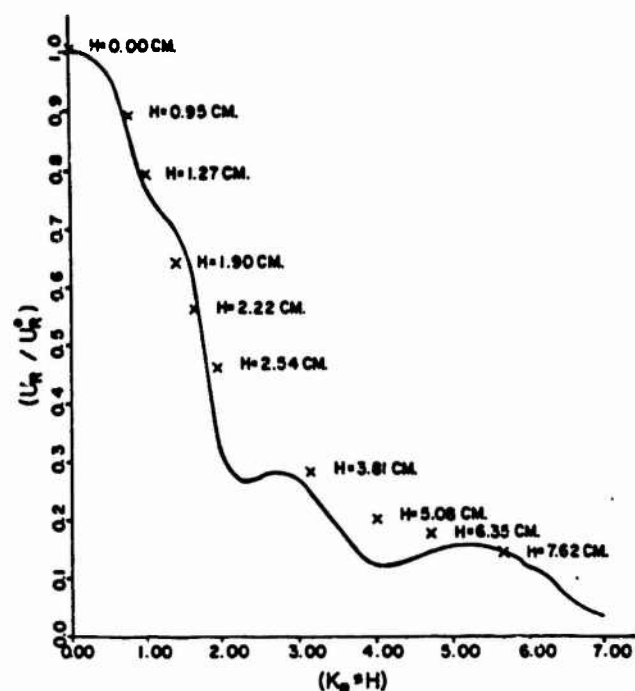
Fig. 1. Comparison of theoretical (———) and experimental results (x) for the amplitude of the transmitted surface wave (from Ref.4).
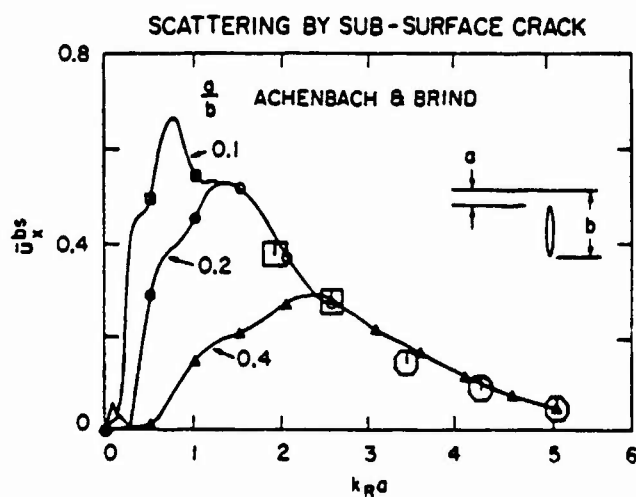

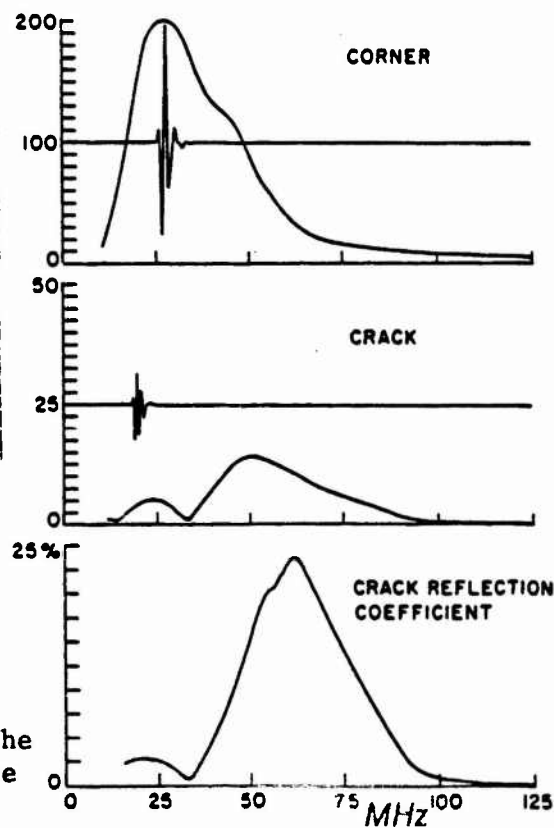Fig. 2. Theoretical results for back-scattering by a sub-surface crack.

Fig. 3. Experimental measurement of the reflection coefficient of a sub-surface crack (Khuri-Yakub et al[5]).

postulated and $u^{sc}(x)$ is subsequently computed by (2.2). At low
frequencies the static crack-opening-displacement can be substi-
tuted in the integral, to give the so-called quasi-static
scattering theory. At very high frequencies the geometrical
elastodynamic field on the illuminated crack-face can be used as
the crack-opening displacement. Subsequent evaluation of (2.2)
produces the "physical elastodynamics" or Kirchhoff approximation
to the scattered field.

3. RAY METHODS FOR CRACK-SCATTERING PROBLEMS

In ray theory it is assumed that disturbances propagate along
straight or curved rays, and that the interaction of rays with
inhomogeneities follows simple geometrical rules which can be
established on the basis of solutions to canonical problems. If
the rules are known, then rays can be traced and (in principle) the
signals that propagate along all rays passing through a point of
observation can be superimposed to yield the complete field. The
geometrical aspects of ray theory have intuitive appeal, and they
are relatively simple. From the mathematical point of view, ray
theory gives an expansion which has asymptotic validity with
respect to "high" frequency or "small" time after arrival of a
disturbance.

The scattering of a bundle of rays by a crack-like flaw
follows relatively simple rules. At sufficiently high frequencies
and outside the zone of specular reflection, diffraction at
certain points on the crack edge, which have been called the "flash
points", produces the dominant part of the scattered field. The
flash points emit bundles of diffracted waves which propagate
towards a point of observation. The basic theory has been pre-
sented by Achenbach, et al[2]. Comparison of theoretical ray theory
results with experimental results has also been given[6].

4. INVERSE RAY TRACING

In the direct problem the incident wave and the geometrical
configuration are known. For a given point of observation the
positions of the flash points on the crack edge can then be
determined by geometrical considerations, and the scattered field
can subsequently be determined by direct ray tracing. If the
geometrical configuration is unknown, but information is available
on the diffracted field, an inverse ray tracing procedure can be
used to determine the flash points on the crack edge from which
diffracted signals have emanated.

In recent papers[7-9] two analytical methods have been developed
to map the edge of a crack by the use of data for diffraction of
elastic waves by the crack-edge. These methods are based on
elastodynamic ray theory and the geometrical theory of diffraction,
and they require as input data the arrival times of diffracted

ultrasonic signals. The first method maps flash points on the crack edge by a process of triangulation with the source and receiver as given vertices of the triangle. By the use of arrival times at neighboring positions of the source and/or the receiver, the directions of signal propagation, which determine the triangle, can be computed. This inverse mapping is global in the sense that no a-priori knowledge of the location of the crack edge is necessary. The second method is a local edge mapping which determines planes relative to a known point close to the crack edge. Each plane contains a flash point. The envelope of the planes maps an approximation to the crack edge. The material containing the crack was taken as a homogeneous, isotropic, and linearly elastic solid. More recently, extensions to include anisotropy of the material have been given in Refs. 10-11. Mathematical details and a fairly detailed error analysis can be found in Ref. 9. References 7-9 also include applications of the methods to synthetic data. It is of particular interest that the local mapping technique allows for an iteration procedure whereby the result of a computation suggests an improved choice of the base point which in the subsequent iteration yields a better approximation to the crack edge. A comparison with experimental data has been given in Ref. 12.

5. CRACK-FACE INTERACTIONS

The results of the preceding Sections are for a perfect mathematical crack, that is, an infinitesimally thin crack, with smooth faces. The effects of crack-face interaction are ignored in consideration of the perfect mathematical crack. However, the failure processes that result in a crack generally produce rough crack faces. Once a crack has been opened and the crack faces have undergone the slightest relative sliding displacement, it must be expected that it will never completely close again due to incompatibility of the rough crack faces. Under subsequent loading conditions the faces of the crack generally may not be free of surface tractions, as is assumed for a perfect mathematical crack, nor will there be perfect contact between the crack faces. Unless the crack faces are completely separated due to a state of pre-stress, a complicated interaction between the crack faces is to be expected, which will be different for opening and closing of the crack on the one hand, and relative sliding of the crack faces on the other. For a slightly closed crack, the interaction of the crack faces will be a non-linear process which will depend strongly on the magnitudes of the tractions transmitted across the contacting crack faces.

The effects of interaction between contacting crack faces are of particular interest in studies of crack detection and crack characterization by the use of the specular reflection and scattering of ultrasonic waves. A perfect mathematical crack acts as a perfect screen for reflection and scattering. A crack with interacting crack faces may be a poor reflector, and thus difficult

to detect and characterize. In recent work[13] it has been assumed that for the purpose of computing the fields of stress and deformation elsewhere in the body, the interaction between the upper and lower faces of the flaw plane can be described by appropriate relations between the tractions and displacement across a perfectly flat surface. This surface may be considered as the median plane of the actual flaw surface. Let us consider a two-dimensional configuration with a flaw plane in the plane $y = 0$, as shown in Fig. 4. In the analytical model we consider averaged tractions and averaged displacement discontinuities per unit area, with respect to coordinates in the flaw plane. The averaged tractions are continuous, which implies that at $y = 0$:

$$\sigma_y^+ = \sigma_y^- = \sigma_y^* , \qquad \sigma_{yx}^+ = \sigma_{yx}^- = \sigma_{yx}^* , \qquad (5.1a,b)$$

where the + and − signs refer to the upper and lower sides of the flaw plane. It should be noted that (5.1a,b) include the conditions for a perfect mathematical crack, which are that the stresses vanish. In the present model for a flaw plane with rough faces, (5.1a,b) will be supplemented by relations between the stresses $\sigma_y^*, \sigma_{yx}^*$, and the displacement discontinuities [v] and [u], respectively.

(a)

(b)

Fig. 4. Schematic depiction of flaw plane.
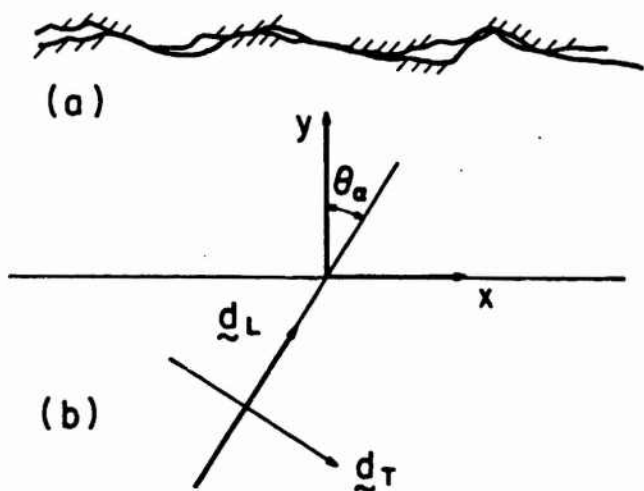
We will first consider the opening mode of the flaw plane. It is reasonable to assume that in the unloaded state, i.e., when $\sigma_y^* = 0$, the faces will be slightly separated: $[v] = \Delta > 0$. In the closing mode we have $\sigma_y^* < 0$, and the required stress will increase rapidly as $[v] \to 0$. In fact we assume that an infinite interface stress σ_y^* is required

to close the flaw plane completely $[v] = 0$, i.e., to completely flatten out the roughness of the faces. The opening displacement cannot be negative since that would imply overlap of the faces. To separate the faces, $[v] > \Delta$, a slight resistance has to be overcome. The behavior described here can be represented by the relation

$$\sigma_y^* = T \frac{[v] - \Delta}{[v]} \qquad (5.2)$$

Here T is the maximum tensile force (very small) that can be transmitted across the faces. Equation (5.2) represents a non-linear spring. It takes into account different behavior for opening and closing. If the flaw plane is already closed a local linear approximation may be adequate, as discussed by Thompson and Fiedler[14].

We have assumed that separation of the flaw-plane faces is independent of sliding of the faces. The opposite, however, can not be assumed. The resistance to sliding depends very much on the magnitude of σ_y^*. When $\sigma_y^* > 0$ there will be very little resistance to sliding, while for $\sigma_y^* < 0$ there will be considerable resistance. A convenient relation between σ_{yx}^* and [u] is that we require $|\sigma_{yx}^*| \leq S$, and

$$[\dot{u}] = \dot{\sigma}_{yx}^* / C \text{ for } |\sigma_{yx}^*| < S, \text{ where } C = \text{constant}, S = S_o \exp(-\alpha \sigma_y^*). \qquad (5.3)$$

Note that the critical value S depends on σ_y^*. The relation that we have assumed satisfies the condition that S is small for $\sigma_y^* > 0$, while S increases rapidly as σ_y^* becomes negative, i.e., as the faces are pressed together. The key point to observe is the possibility of displacement hysteresis. The parameters $T, \Delta, C, \alpha,$ and S_o have to be determined from the crack geometry and from experimental data.

Equations (5.1)-(5.3) account for crack closure and for the related resistance to crack-face sliding. In Ref. 13 the relations have been used to investigate reflection and transmission of an incident pulse by an infinite flaw plane. Because of the nonlinearity the analysis had to be carried out directly in the time domain. The problem statement was reduced to a set of inhomogeneous nonlinear ordinary differential equations for the displacement discontinuities, [u] and [v], across the flaw plane. These equations were solved numerically. The reflected and transmitted displacement pulses then follow directly from [u] and [v]. Next the Kirchhoff approximation in the time domain was used to derive expressions for the specular reflection and transmission of an incident pulse by a crack with intersecting crack faces. Both incident longitudinal and transverse waves were considered. The loss of specular reflection as compared to a perfect (traction-free) crack has been exhibited by specific examples.
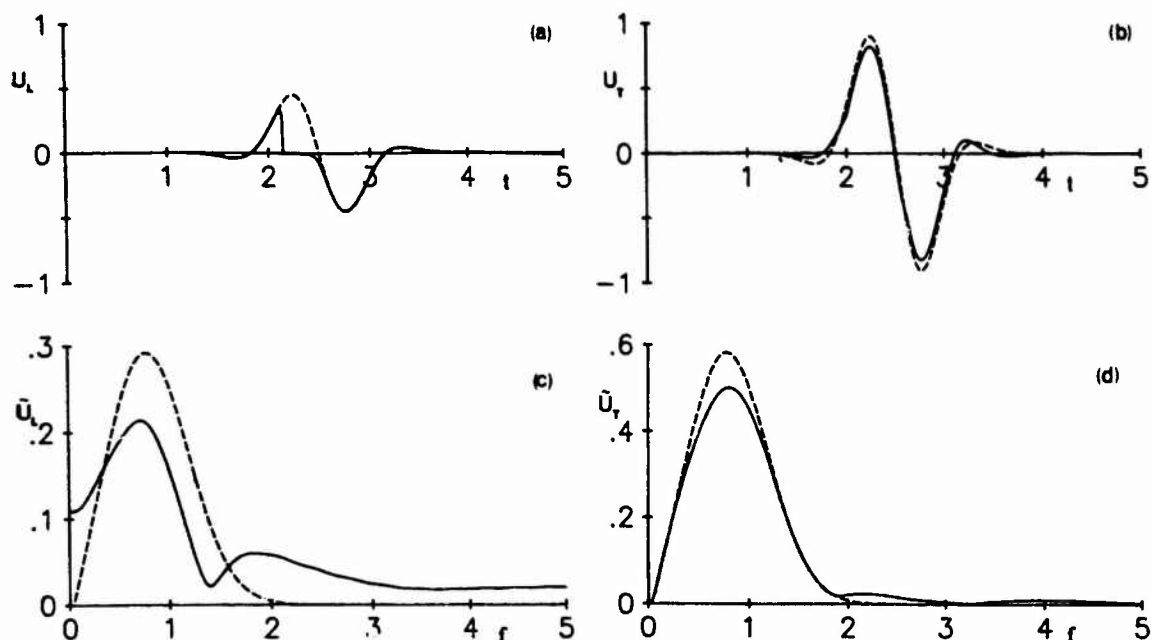
Fig. 5. (a) and (b), Far-field amplitudes for normally incident
L and T-waves, respectively. (c) and (d), Spectra of (a) and (b).

In Figs. 5a and 5b we have plotted the far-field amplitudes for
wave incidence on a crack. The discontinuity in U_L is related to
the rapid closure of the crack. The dashed curves in Fig. 5 are
the same amplitudes for the stress free crack. Also plotted in
Figs. 5c and 5d are the magnitudes of the Fourier transforms of
U_L and U_T.

6. FLAW PLANE OF PERIODICALLY SPACED MICROCRACKS

In Ref. 15, the interaction of elastic waves with a planar
array of periodically spaced cracks of equal length was investi-
gated. Normal incidence of both longitudinal and transverse waves
was considered. The geo-
metry is shown in Fig. 6.

Fig. 6. Array of cracks.

At some distance from the
plane of the cracks, the
displacement fields appear
as the superposition of a
finite number of reflected
and transmitted plane-wave
propagating modes. The
reflection and transmission
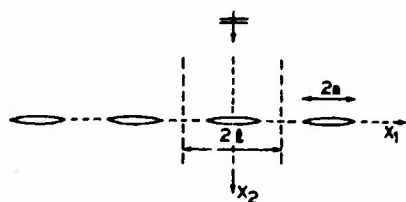coefficients corresponding
to the propagating mode of
order zero were computed for various values of the frequency and
the ratio of the crack length to the crack spacing. The results

are comparable to those obtained for scattering of elastic waves by surfaces with periodic roughness. The results of Ref. 15 can also be brought into perspective with investigations for the reflection of elastic waves by a flaw plane, when the flaw plane is viewed as a region where separation zones and contact zones can both exist, and friction may be significant over the contact zones. As discussed in Section 5, Achenbach and Norris[13] have proposed a set of non-linear boundary conditions to account for the separation and friction effects. Other boundary conditions, of a linear type, are discussed by Thompson and Fiedler[14]. In Ref. 15 it is assumed that the separation zones are not affected by the action of the incident wave. The displacements as well as the stresses are continuous over the plane regions in between the cracks. Hence, the configuration models an interface with predetermined separation zones and very rough contact zones.

The total field in the solid can be analyzed as the superposition of the incident field in an uncracked space and the scattered field in the cracked space. The scattered field is generated by prescribed surface tractions on the faces of the cracks which are equal in magnitude, but opposite in sign, to ᴜ..e tractions of the incident wave. Because of the periodicity of the excitation and of the boundary conditions, the field variables take periodic values. The mixed-boundary value problem for a typical strip is reduced to a singular integral equation of the first kind for the dislocation density across the crack faces. The integral equation was solved numerically. There are certain frequencies for which the integral equation does not hold. At these frequencies, a pair of integral equations is needed to describe the behavior of the system properly. The balance of rates of energies, which involves the incident wave as well as the reflected and transmitted propagating modes, is obtained for all frequencies. The reflection and transmission coefficients are easily computed once the dislocation density is known.

Figure 7 shows the reflection coefficients versus $2\ell/\lambda_T = \omega\ell/\pi c_T$. In Fig. 8 the exact theory is compared with two approximate theories. The first theory is a static limit to the dynamic theory. The second one is inspired by Thompson and Fiedler's paper[14], where the array of cracks is replaced by an equivalent spring-layer. Both approximations agree with the exact theory at low frequencies.

7. THE EFFECT OF ANISOTROPY

We conclude with a brief discussion of the problem of scattering by a stress-free crack in an anisotropic solid. In practice, many materials exhibit some form of anisotropy. Examples of transversely isotropic solids are laminated media with periodic layering (on a length scale much larger than the characteristic thicknesses of the layers), and metals that have been subjected to
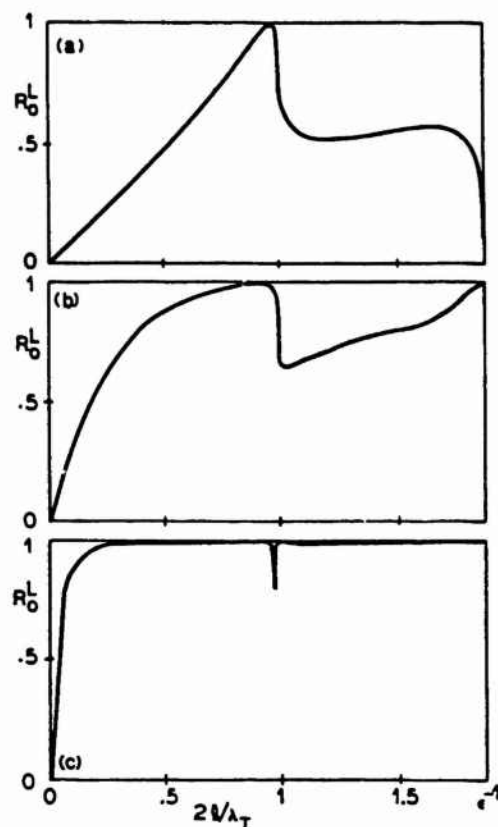
Fig. 7. Reflection coefficient versus frequency for (a) a/ℓ = .5,
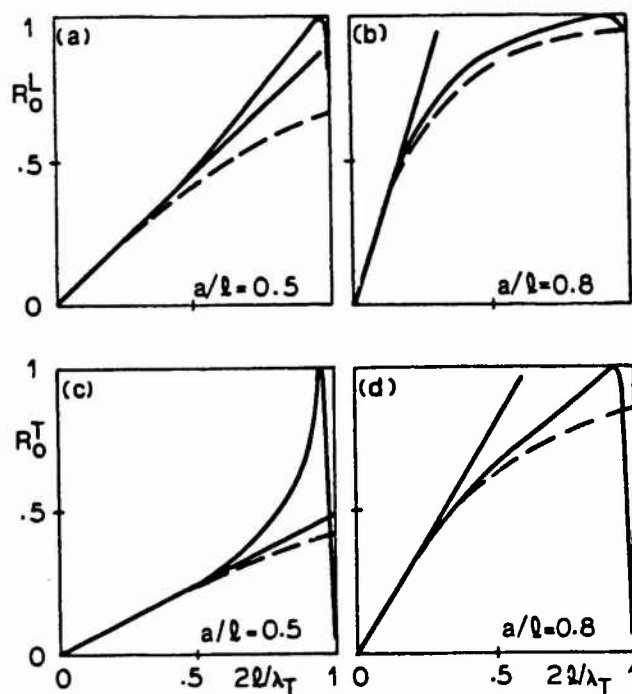(b) = .8, and (c) = .9999; ν = 0.3, incident longitudinal wave.

Fig. 8. Reflection coefficient versus frequency for an incident
longitudinal wave (a,b) and an incident transverse wave (c,d);
straight solid lines: static approximation; dashed lines: spring-
layer approximation; curved solid lines: exact results: ν = 0.3.

certain manufacturing processes (e.g., rolling). Anisotropy may also be induced in an isotropic solid by large prestressing or straining.

The number of known solutions for scattering problems in anisotropic solids is much smaller than for isotropic elasticity. The present discussion, which is based on Ref. 16, is concerned only with the direct scattering from cracks in transversely isotropic solids. The inverse problem of locating and sizing a crack in anisotropy has been discussed in Ref. 10.

We first consider a semi-infinite crack located in a plane of symmetry of a transversely isotropic material. The incident wave motion is confined to the plane which is normal to the crack edge. Therefore, the scattering geometry is two dimensional. This problem can be viewed as a canonical problem whose solution is necessary for the computation of the diffraction coefficients, and development of an anisotropic geometrical theory of diffraction (GTD).

Now, let a plane quasi-longitudinal wave of unit amplitude be incident at angle θ with the plane of the crack, on a crack of finite length D which is located in a plane of symmetry. The diffracted quasi-longitudinal field in the back scattered direction can then be computed by using the diffraction coefficient for each tip of the crack individually. Superposition of the two crack-tip diffractions gives a high-frequency approximation to the back scattered or pulse-echo signal. It is assumed that D is of the same order as the wavelength.
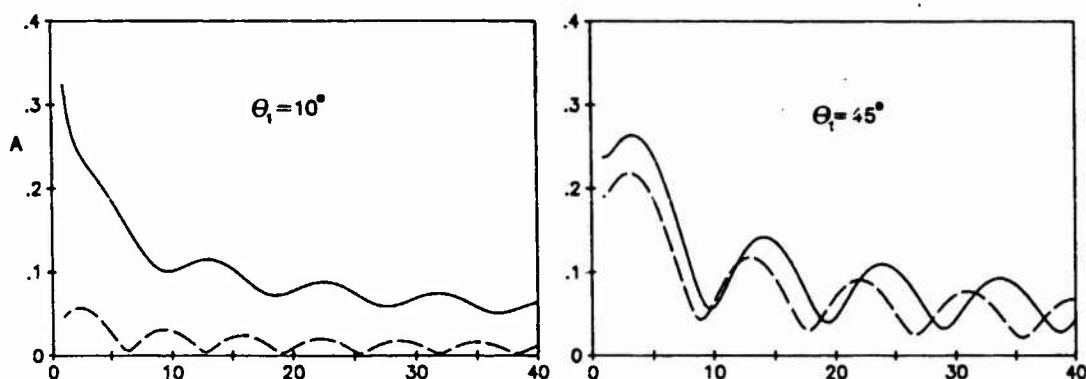

Fig. 9. Backscattered amplitude from a finite crack. Dashed line is the isotropic result. $k = D\omega/\sqrt{b}$.

Taking the origin at the center of the crack, the far field amplitude $A \equiv |(r/d)^{\frac{1}{2}} \underline{u}(r,\theta)|$ has been plotted in Fig. 9 as a function of the dimensionless frequency $D\omega/\sqrt{b}$. We note that $\omega/\sqrt{b}$ is the longitudinal wave number in the direction normal

to the slit ($\theta = \pi/2$). The isotropic result ($a/d = 4$) is also plotted in Fig. 9 for comparison. Because b is the same for the two examples, the effect of anisotropy disappears at normal incidence.

Figure 9 shows that the anisotropy is important, especially at angles of incidence near grazing.

CONCLUDING COMMENT

In this paper some elements of direct and inverse crack-scattering problems have been summarized, with a view towards applications to quantitative non-destructive evaluation. For details the reader is referred to the cited references.

ACKNOWLEDGMENT

REFERENCES

1. J.D. Achenbach, Wave Propagation in Elastic Solids (North-Holland Publishing Co., Amsterdam-New York, 1973).
2. J.D. Achenbach, A.K. Gautesen and H. McMaken, Ray Methods for Waves in Elastic Solids (Pitman Advanced Publishing Program, Boston, London, Melbourne, 1983).
3. J.D. Achenbach, Y.C. Angel and W. Lin, in Proc. AMD/ASME Symposium on Wave Propagation in Inhomogeneous Media and Ultrasonic NDE, (1984), p. 93.
4. C.H. Yew, K.G. Chen and D.L. Wang, J. Acoust. Soc. Am., 75, 189 (1984).
5. B.T. Khuri-Yakub et al, in Review of Progress in Quantative Nondestructive Evaluation, Vol. 3, (ed. by D.O. Thompson and D.E. Chimenti), Plenum Press, New York, (1984), p. 229.
6. J.D. Achenbach et al, J. Acoust. Soc. Am., 66, 1848 (1979).
7. J.D. Achenbach and A.N. Norris, in Review of Progress in Quantitative Nondestructive Evaluation, Vol. 1, (ed. by D.O. Thompson and D.E. Chimenti), Plenum Press, New York (1982), p. 491.
8. J.D. Achenbach, A.N. Norris and K. Viswanathan, Bull. Seism. Soc. Am., 72, 779 (1982).
9. A.N. Norris and J.D. Achenbach, J. Acoust. Soc. Am., 72, 264 (1982).
10. A.N. Norris, J. Acoust. Soc. Am., 73, 421 (1983).
11. A.N. Norris, in Review of Progress in Quantitative NDE, Vol.2, Plenum Press, (1983), p. 907.
12. J.D. Achenbach et al, in Review of Progress in Quantitative NDE, Vol. 2, Plenum Press, (1983), p. 1097.
13. J.D. Achenbach and A.N. Norris, J. of Nondestructive Evaluation, 3, 229 (1982).

14. R.B. Thompson and C.J. Fiedler, in Review of Progress in Quantitative NDE, Vol. 3, Plenum, New York, (1984) p. 207.
15. Y.C. Angel and J.D. Achenbach, J. Appl. Mech. in press.
16. A.N. Norris and J.D. Achenbach, Q.J. Mech. and Appl. Math, in press.

ANALYSIS AND SYNTHESIS OF OPTIMIZED EDDY CURRENT PROBES

B. A. Auld
Edward L. Ginzton Laboratory
Stanford University
Stanford, California 94305

ABSTRACT

The aim of this presentation is to give a coherent review of eddy current probe design, with emphasis on task-oriented choices of probe geometry. Flaw detection and sizing optimization is discussed with respect to detection sensitivity and accuracy of inversion, taking probe geometry and operating frequency as design parameters. The theoretical base for these procedures is presented, together with recent experimental comparisons of theory and experiment, including measurements of probe field distributions and methods for utilizing these measurements in predicting probe performance.

I. COMPARISON OF EDDY CURRENT AND ULTRASONIC METHODS

Since the principles of ultrasonic testing are now much more widely understood than those of eddy current testing, it is useful to begin by comparing the physical principles and the numerical magnitudes of the parameters. In both cases the flaw interacts with fields excited by the transducer (or probe) and the flaw response can be described in principle as a scattering process. Figure 1 illustrates the electromagnetic (or eddy current) detection process from this point of view. To emphasize the scattering viewpoint the transmitting and receiving transducers are taken to be small horn antennas operating at about 1000 Mhz. At this frequency the wavelength in air is approximately 30 cm, comparable to the dimensions of the horns. In the metal workpiece, on the other hand, the wavelength is about 15 microns (in aluminum). This corresponds to a phase velocity of 15000 m/s, much smaller than in air but considerably larger than the velocity of an ultrasonic wave. The attenuation of the electromagnetic wave in the metal is very high, leading to a penetration depth of only 2.5 microns at this frequency. Electromagnetic testing of metals at high frequencies is therefore suitable only for surface flaws. Because of this fact, and the high velocity of the wave in the metal, a pulse echo experiment gives a very close-in response. A further difficulty with pulsed electromagnetic testing is that propagation in the metal is very dispersive, leading to severe distortion of the pulses. Nevertheless, pulsed electromagnetic techniques are used in practice, but in a very different way than in ultrasonics. In this paper, only continuous wave testing will be discussed. Here, the principle effect of the parameters being greatly different than in ultrasonic testing is the extreme degree of refraction occurring at the interface (Fig. 1). The difference in phase velocities in air and in metal is so great that a scale drawing of the refraction angle is not possible, but this figure does give an idea of the effect. In pulsed ultrasound the effect of refraction is to change the angles of the incident and scattered beams at the flaw. This is not relevant for continuous wave electromagnetic testing. Here, as will be seen below, the important factor is the shape of the "interrogating field," i.e., the field of the probe in the absence of the flaw. Because of the strong refraction at the interface, this field is very different from the field of the probe in air, and an important part of quantitative electromagnetic testing is concerned with characterizing the probe field and determining its effect on
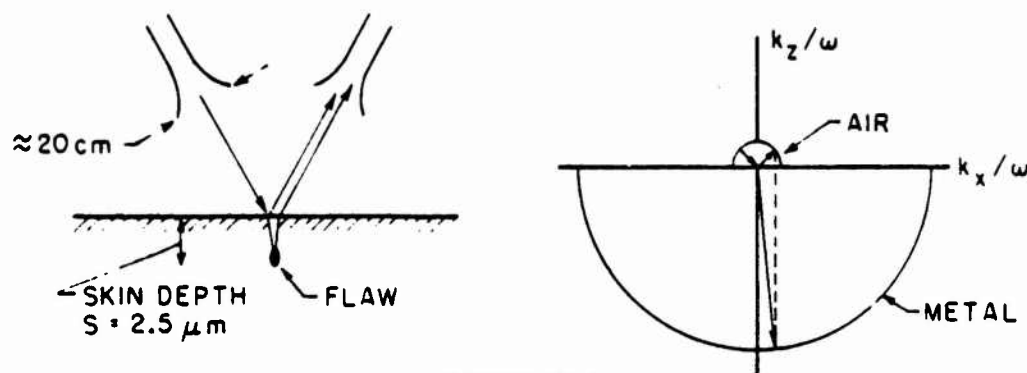
1

FIGURE 1

An Eddy current "scattering" experiment.

the interaction of the probe and the flaw.

Very little electromagnetic (or eddy current) testing is performed at frequencies in the range of 1000 Mhz. Typically, operation is in the range of a few hundred kiloherz to a few megaherz. Figure 2 shows a basic probe geometry. The probe consists of a multiturn coil placed very close to the surface. In aluminum the field penetration depth into the workpiece is approximately 0.25 mm at 500 kiloherz. It varies inversely with the square root of the frequency, so that lower frequencies are required for flaws in the interior of the workpiece. The effec' of changing frequency are, however, much more complicated than this. A very important parameter in determining the nature of the interaction between the probe and a flaw is the ratio of a characteristic dimension a of the flaw to the penetration depth (or skin depth) δ. The ratio of a characteristic dimension of the probe itself to the skin depth is also important in that it has a significant influence on the shape of the interrogating field in the work piece. Figure 3 gives a graphic example of an ultrasonic transducer operating under conditions typical of eddy current testing—i.e., a transducer of dimensions small compared with the wavelength in the water bath, plus a workpiece of material with high loss and velocity much smaller than that of the bath and placed in the very near field of the transducer. In this situation the field at the flaw is highly nonuniform unless the flaw is very much smaller than the probe—a situation that makes the theoretical problem much more difficult than in ultrasonics. Furthermore, difficulties arise in calculating the field of the probe in the presence of the workpiece. If the workpiece is perfectly conducting its presence can be accounted for by using image theory (Fig. 3). Over an imperfect conductor there is a single image of the probe, and Fourier transform methods are used to find the interrogating field.[1]

II. THEORY OF EDDY CURRENT PROBE-FLAW INTERACTION

The first derivation of an eddy current detection formula was presented by Burrows in 1964 (Fig. 4).[2] It is for a transmission probe geometry and applies to ellipsoidal inclusions that are small compared with the skin depth. This formula gives the important result that the flaw response is proportional to the product of the normalized transmitter and receiver coil fields at the position of the flaw. Part (c) of the figure gives the form of the formula for the particular case of a magnetic inclusion. The restriction to
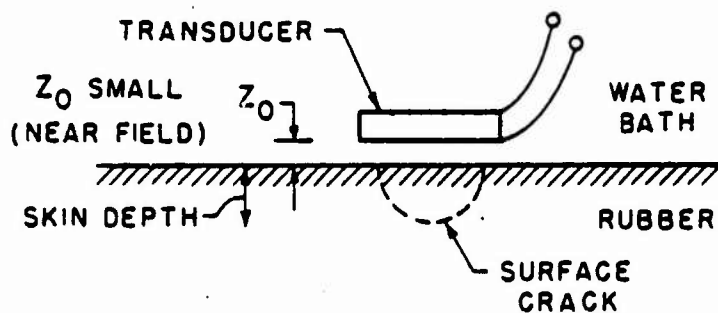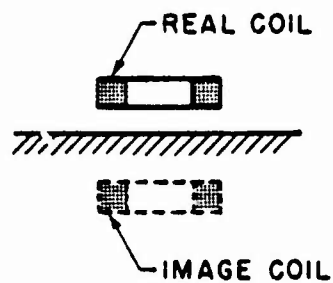
2
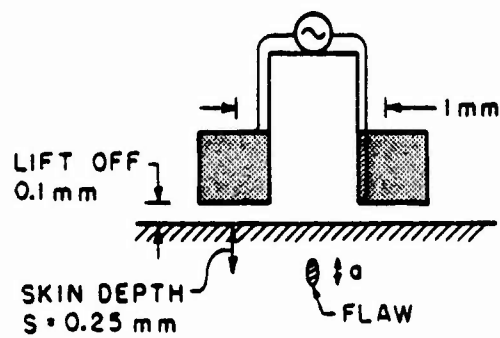
FIGURE 2

Typical eddy current probe geometry.

EQUIVALENT ULTRASONIC TRANSDUCER PROBLEM
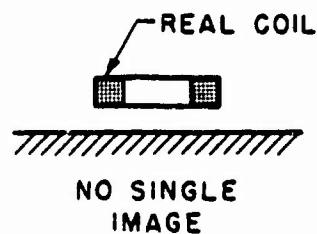

IMAGE PROCEDURE FOR EC TRANSDUCER

PERFECT CONDUCTOR

IMPERFECT CONDUCTOR

FIGURE 3

An "equivalent" ultrasonic transducer problem.

BURROWS EC FORMULA (1964)

(a)
T-COIL
I_T

ELLIPSOIDAL
MAGNETIC
INCLUSION

H_T AT FLAW

DIMENSION $a \ll$ SKIN DEPTH "δ"

(b)
R-COIL
+ −

INDUCED VOLTAGE

$V_R \sim M_F$

(c)

$$Z_{RT} = \frac{V_R}{I_T} \sim \left(\frac{H_T}{I_T}\right)\left(\frac{H_R}{I_R}\right) K_F\,(\delta\mu)$$
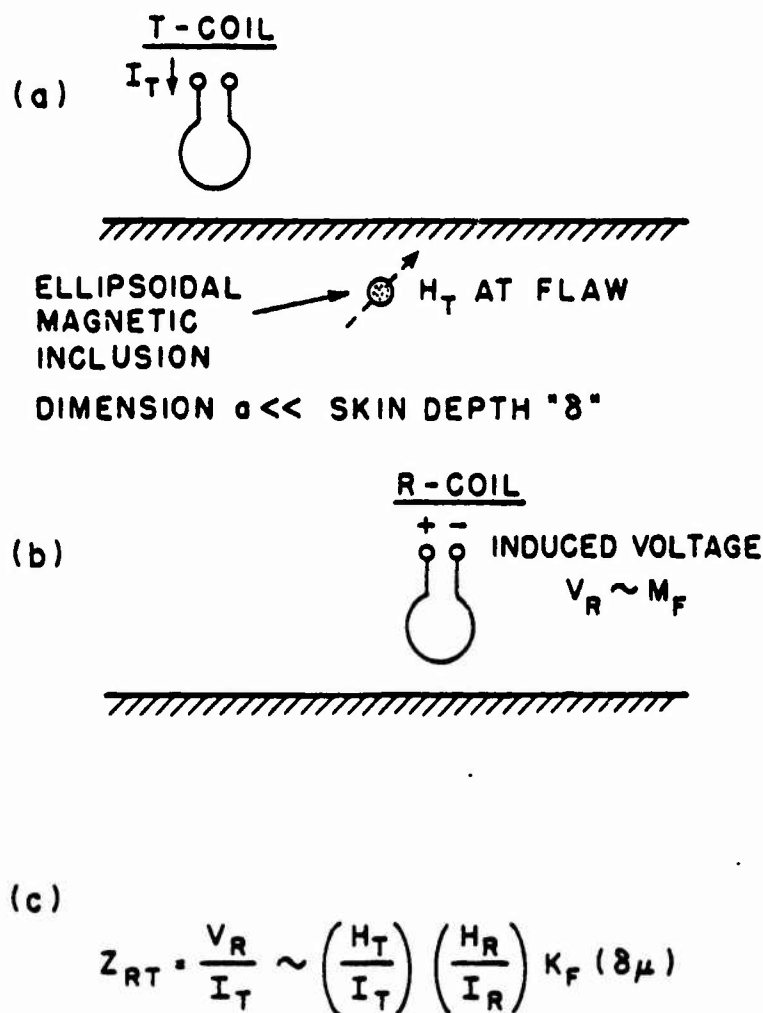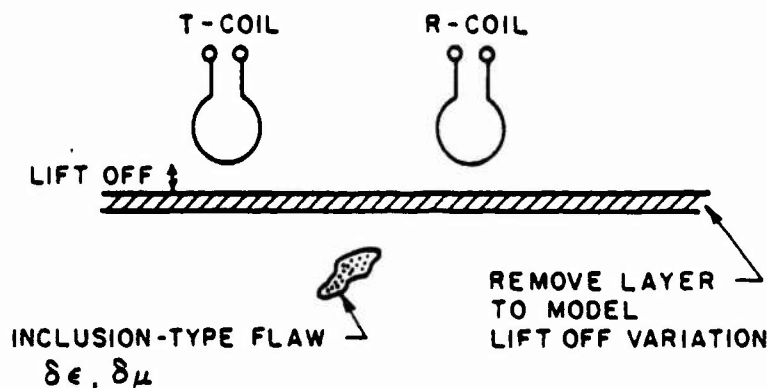
FIGURE 4

The basic eddy current detection formula.

a small flaw of ellipsoidal shape is a very severe limitation in practical problems, but it can be removed by applying the Lorentz reciprocity relation to the problem (Fig. 5).[3] In the formula of the figure the unprimed fields are those existing in the unflawed workpiece—i.e., the interrogating field—and the primed fields are those existing in the presence of the flaw. As given in the figure, the eddy current formula requires the inclusion to be neither of ellipsoidal shape nor small compared with the skin depth and the probe. The same formula can be used to evaluate the effect of variations in the height of the probe above the surface of the workpiece. The signal arising from such changes, called liftoff, is the dominant spurious signal limiting the sensitivity of detection in eddy current testing. It is an important factor in probe design. To apply the formula of Fig. 5 to the calculation of liftoff, the "flaw" is taken to be a particular

4

GENERAL RECIPROCITY FORMULATION

$$Z_{RT} = \frac{1}{I_T I_R} \int_{FLAW} \left\{ \vec{E}_R \cdot \delta\epsilon \, \vec{E}_T^{\,\prime} - \vec{H}_R \cdot \delta\mu \, \vec{H}_T^{\,\prime} \right\} dV$$

UNPRIMED – NO FLAW
PRIMED – WITH FLAW

FIGURE 5

General reciprocity relation formulation of eddy current detection.

type of void consisting of the removal of a layer from the surface. (In using the formula for a void the changes in material parameters within the flaw—$\delta\epsilon$ and $\delta\mu$—are the differences between the parameters of air and those of the workpiece).

The formula given in Fig. 5 is suitable for inclusions and voids of finite volume, but not for thin cracks. For this class of flaw the reciprocity relation derivation is cast into the form of a surface integral. As applied to a single coil (or absolute) probe (Fig. 6), this approach leads to[2]

$$\Delta Z = \frac{1}{I^2} \int_{S_F} (E \times H' - E' \times H) \cdot \hat{n} \, dS \tag{1}$$

where the primed and unprimed fields have the same meaning as in Fig. 5. This is an exact result and has no restrictions on the size or shape of the flaw. It can be used for all types of flaws, even inclusions and voids, but it is particularly well-suited to tight cracks and liftoff. The basic problem in applying it is to evaluate the primed fields on the surface of integration, which is arbitrary so long as it completely encloses the flaw. In some cases it is most convenient to take this surface as the boundaries of the flaw but, for surface cracks, it will be seen in Section V that a more suitable choice is the surface of the workpiece (Fig. 6). This is also a good choice for liftoff calculations.
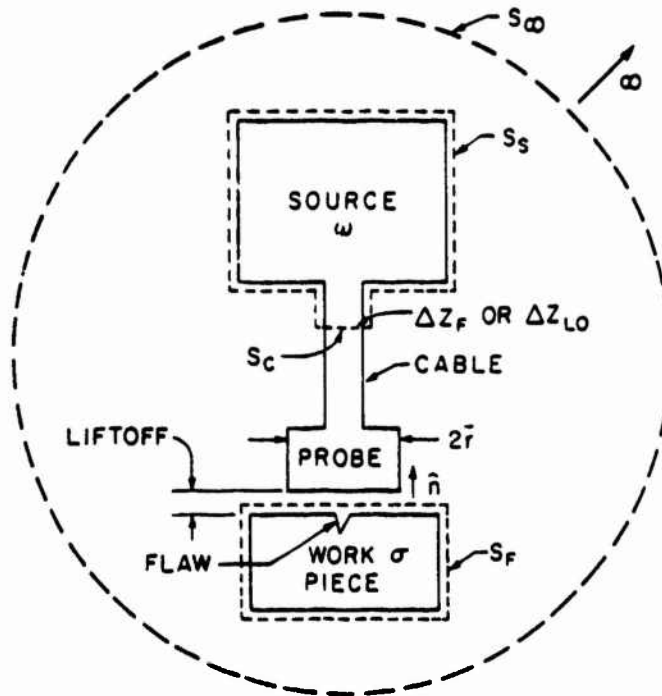
5

FIGURE 6

Surface integral formulation of the eddy current signal for an absolute-type eddy current probe.

III. FACTORS INFLUENCING THE INTERROGATING FIELD

Equation (1) can be recast in a form that explicity displays the interrogating field,[2,3]

$$\Delta Z = \int_{S_F} \left[\underbrace{\frac{H^2_{tan}(x,y,\omega,\sigma)}{I^2}}_{Interrogating Field} \right] \left\{ \begin{array}{c} Characteristic \\ Function \end{array} \right\} dS \qquad (2)$$

Here, the surface of integration is the surface of the workpiece, as in Fig. 6, and is effectively restricted to the upper face of the workpiece near the flaw, unless the flaw is close to an edge. The reason for this restriction is that a typical probe (Fig. 2) is much smaller than an electromagnetic wavelength in air. It therefore has almost no radiation and its magnetic field, being described by quasistatic equations, dies away rapidly with distance from the probe. In Eq.(2) x and y are coordinates in the top face of the workpiece, and the tangential H field in the first term of the integrand is a component of field parallel to the workpiece surface in the absence of the flaw—i.e., it is the *interrogating field*. The second term of the integrand is the characteristic function of the flaw, containing information about its shape and dimensions. As in Eq. (1), this formula can be used for both tight cracks and liftoff effects.

Equation (2) explicitly displays the role played by the interrogating field in controlling the probe-flaw interaction. The flaw response may be described as a projection of the characteristic function onto the interrogating field. This fact defines the
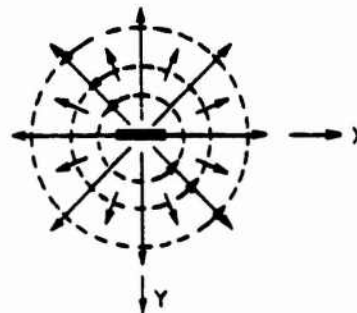
6

(a) NORMAL PROBE

STRUCTURE
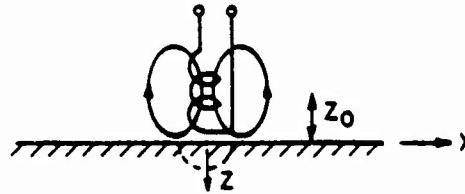
SURFACE
EDDY CURRENT
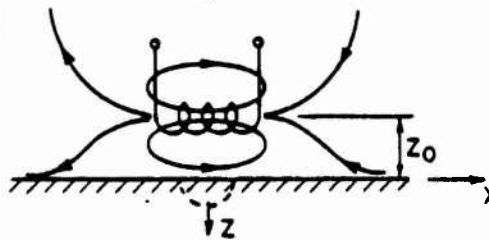STREAM LINES
- - - - - - →
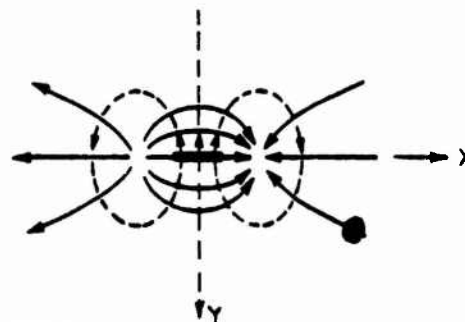
(b) PARALLEL PROBE

STRUCTURE

SURFACE
EDDY CURRENT
STREAM LINES
- - - - - - →

FIGURE 7

Two basic air core probe configurations.

relationship between probe design and flaw response optimization. The interrogating field is controlled by two factors: (a) probe geometry, (b) workpiece conductivity, and (c) operating frequency. Figure 7 shows two different probe geometries based on the simple air-cored absolute probe, one with the coil axis vertical and the other with it horizontal.[4] Figure 8 shows the same two geometries for a ferrite-cored absolute probe. It is clear from Fig. 7 that the vertical coil has an interrogating field that is much more highly nonuniform. In fact even a very small flaw placed directly at the center of the tangential magnetic field pattern (solid arrows) in part (a) of the figure sees a

7

(a) VERTICAL   (b) HORIZONTAL

FIGURE 8

Ferrite core probes corresponding to the two types in Fig. 7.

very nonuniform field. By contrast, the same small flaw placed at the center of the field pattern in part (b) of the figure sees a quite uniform field. From Eq. (2) this will have a pronounced influence on the probe responses to both flaws and liftoff. It was noted earlier, in connection with Fig. 3, that analysis of the interrogating field over a workpiece with finite conductivity is carried out in the Fourier transform plane. The effect of the workpiece on the individual Fourier components is controlled by both the conductivity of the material and the operating frequency of the probe, so that the same probe can have significantly different interrogating fields over different workpieces and at different frequencies (Reference 1). This means that special care must be taken in characterizing the field of an eddy current probe (Section IX).

IV. LIFTOFF DISCRIMINATION

The liftoff signal is typically orders of magnitude larger than the flaw signal and must be well suppressed. Three techniques are commonly used: (a) accurate height control by means of spring loading, an air bearing, or some feedback system; (b) phase discrimination; and (c) balanced probe construction. Figure 9 illustrates the principle of phase discrimination. It is found experimentally, and confirmed by theoretical modeling, that a flaw signal and a liftoff signal have different phase angles in the impedance plane. For the absolute type of probe under discussion the "signal" consists of a change in the input impedance of the probe. This is detected by placing the probe in a balanced impedance bridge and observing the change in bridge output voltage in both magnitude and phase. The output is displayed with its real and imaginary components on the vertical and horizontal axes of a picture tube. In this visual display of the probe impedance changes the spot moves in a different angular direction when the probe moves over a flaw than it does when the probe liftoff is changed. To exploit this effect in discriminating against liftoff the electronics are arranged to permit rotation of the display. The liftoff signal trajectory is then oriented along the horizontal axis as shown in Fig. 9, where part (a) is for a low frequency probe (100 Khz) and part (b) is for a microwave probe (1000 Mhz). The flaw signal is then measured in the vertical (quadrature, Q) channel of the picture tube, while the liftoff signal is primarily in the horizontal (in-phase, I) channel. In this procedure, only the component of the flaw signal that is 90° out of phase with the liftoff is measured. For high detection sensitivity, optimum probe design requires choosing the geometry and operating frequency to obtain

maximum flaw/liftoff ratio in the Q channel of Fig. 9. Since the liftoff, as well as the flaw signal, depends on frequency (Fig. 10) this is a multiparameter optimization. A third procedure for improving liftoff discrimination is to use a balanced probe. The simplest version of this is the differential probe, which consists of two identical coils that are connected in opposite arms of the detection bridge. Liftoff produces identical impedance changes in the two coils. This does not unbalance the bridge and does not produce an output signal, unless the probe is tilted.

V. PROBE-FLAW INTERACTION MODELING

The problem in applying Eq. (1) to the analysis of flaw response lies in evaluating the primed fields around the complicated shape of an actual surface crack. Even for idealized shapes, such as semi-circular or semi-elliptical flat cracks, approximations or purely numerical methods must be used. Analogies can sometimes be used to advantage. Two versions of the hydrodynamic analogy are useful in the limits of low a/δ and high a/δ (Fig. 11). The top of the figure makes use of the fact that the current flow in this case approximates very well the flow of a nonviscous fluid around an obstacle. In Fig. 12 this analogy is exploited in deriving a low frequency inversion procedure that exactly parallels a popular inversion method in ultrasonic nondestructive testing. Unfortunately, the method is not useful in eddy current testing because the phase angle between the flaw signal and liftoff is small in this region and there is consequently no liftoff discrimination. Another, much more useful, hydrodynamic analogy is illustrated in part (b) of Fig. 11. In this case, where the skin depth is much smaller than the depth of the surface crack, it has been shown that the electric field on the top surface of the workpiece and on the faces of the crack is derivable from a potential function that satisfies the two-dimensional Laplace equation. This means that the electric field in and near the crack has streamlines and equipotential functions as shown on the unfolded crack structure in the figure. It turns out that this is exactly a well-known hydrodynamic problem with an analytical solution for the case of the semi-circular (half-penny) crack. This result can be used to calculate the flaw signal of a semi-circular surface crack interrogated by a uniform eddy current field.[3]

To explain the method used for modeling the interaction between an eddy current probe and a three-dimensional surface crack, it is best to begin with a two-dimensional surface crack in a uniform field (Fig. 13). The theory to be described is strictly applicable only to the large a/δ regime, but experimental results show that it gives quite good agreement for a/δ as small as 1.5. As was noted above, the small a/δ regime is not as interesting practically because of it$^{\cdot}$ poor liftoff discrimination. Figure 13 illustrates the two-dimensional crack geometry and the formula for the change in probe input impedance due to the crack. In deriving this formula Eq. (1) was used, with the surface integral performed over the top face of the workpiece. The magnetic field in the mouth of the flaw is approximated by the field on the surface of the workpiece in the absence of the flaw. To calculate the electric field in the mouth of the flaw, a line integral is performed around a loop comprising the walls and mouth of the flaw. This line integral is related to the applied magnetic field through Maxwell's equations, In addition, the current flow around the lips and the tip of the crack are modeled according to Kahn's analysis. Details are given in Ref. 3. In the figure, the different terms in the ΔZ formula are labelled according to their physical origins. The same approach has been followed for a semi-circular surface crack, using the field modeling of Fig. 11(b).
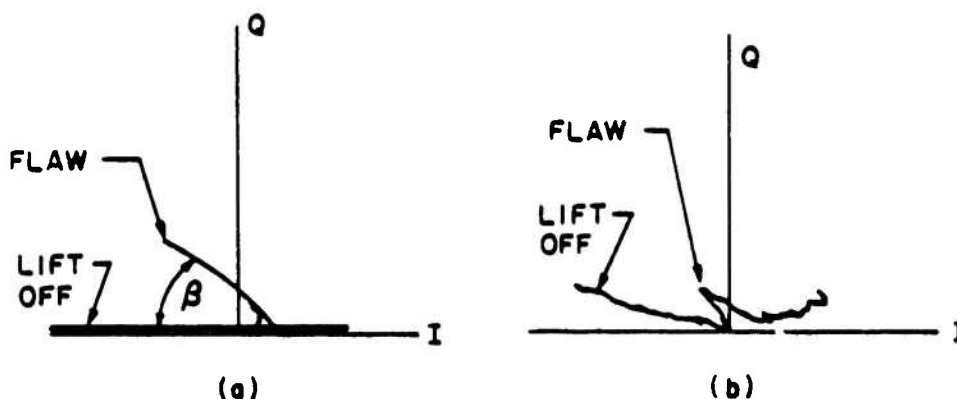
9

FIGURE 9

Phase discrimination between flaw and liftoff signals.

PHASE AND MAGNITUDE OF NORMALIZED 1ST ORDER LIFTOFF

(I - CHANNEL VALUES)

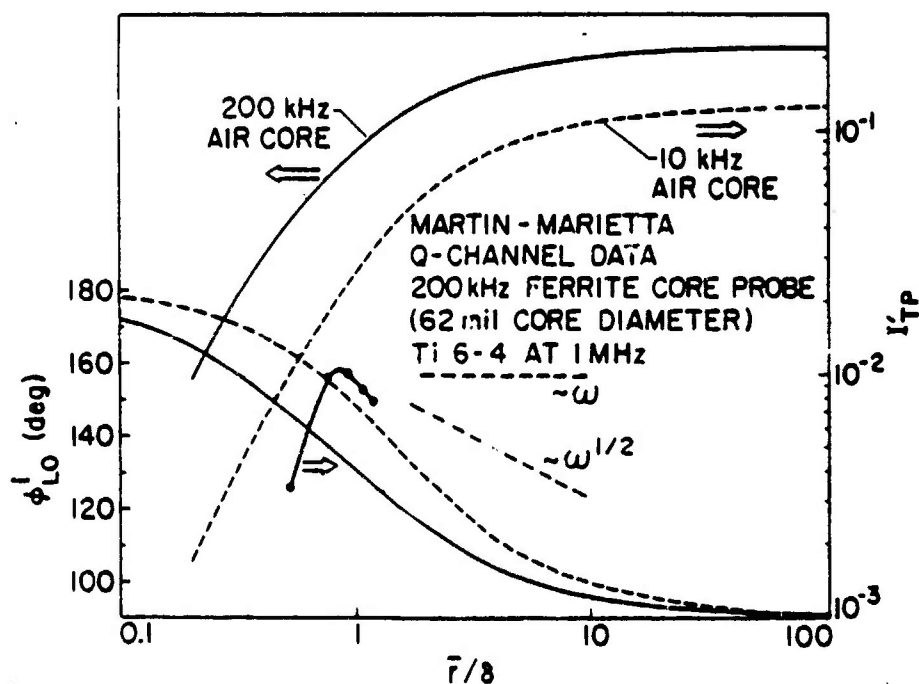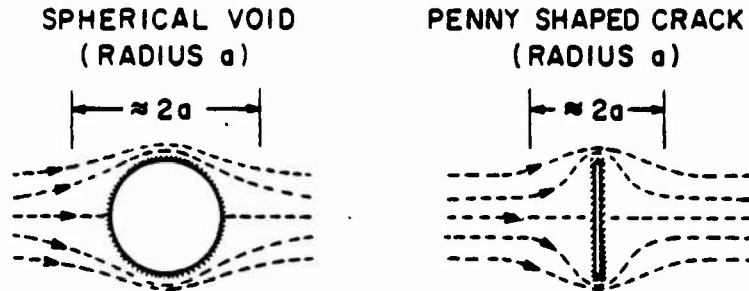Programmed and calculated from
Dodd and Deeds analysis by SRI

FIGURE 10

Phase and magnitude of the first order liftoff signal as a function frequency.

10

3-D FLAWS

(a) LOW a/δ — HYDRODYNAMIC ANALOGY

SPHERICAL VOID (RADIUS a)   PENNY SHAPED CRACK (RADIUS a)

(b) HIGH a/δ — W. D. DOVER et al "UNFOLDING" TECHNIQUE

ANY PART-CIRCULAR CRACK
COAXAL COORDINATES

SURFACE VIEW OF HALF PENNY CRACK   UNFOLDED CRACK STRUCTURE
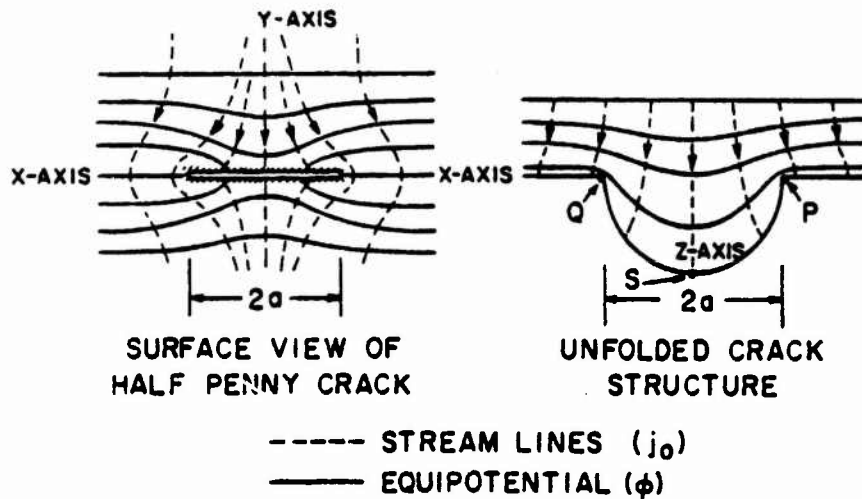
----- STREAM LINES (j_o)
——— EQUIPOTENTIAL (ϕ)

FIGURE 11

Comparison of eddy current flow in the low and high a/δ regimes.

Results of this calculation are given in Ref. 3. The case of a semi-circular surface crack is much too restrictive for practical use. What is actually needed for modeling of real fatigue cracks is a semi-elliptical surface crack, where the ratio of the depth a to the surface length $2c$ is a variable parameter. This problem has not yet been solved, and current modeling of surface cracks is based on the rectangular crack geometry (Fig. 14),[5] which will be discussed more fully in Sections VII and VIII below.
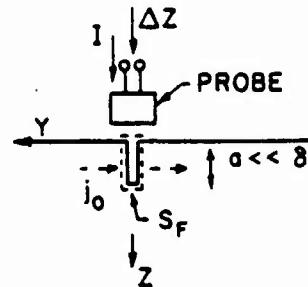
11

NDE INVERSION FOR SMALL SEMICIRCULAR SURFACE CRACKS

STRESS INTENSITY FACTOR $k_I = 2\sqrt{a/\pi}$

(a) **EDDY CURRENT** $(a/\delta \ll 1)$

$$\Delta Z = \frac{1}{I^2}\int_{S_F'} \Delta\phi\, \underline{j}_0 \cdot \hat{\underline{n}}\, dS$$

$$\Delta\phi' = 2j_0\, \frac{2}{\pi}\, \frac{1}{\sigma}\, (a^2 - r^2)^{1/2}$$

$$\Delta Z = \frac{4}{3}\left(\frac{\pi}{4}\right)^3 k_I^6\, \frac{1}{\sigma}\left(J_0/I\right)^2$$

(b) **ULTRASOUND** $(a/\lambda_R \ll 1)$

$$\Delta\Gamma = \frac{i\omega}{4P}\int_{S_F'} \Delta\underline{u}' \cdot \underline{\underline{T}} \cdot \hat{\underline{n}}\, dS$$

$$\Delta u'_{YY} = 2T_{YY}\, \frac{2}{\pi}\, \frac{1-\nu}{\mu}\, (a^2 - r^2)^{1/2}$$

$$\Delta\Gamma = \frac{i\omega}{3}\left(\frac{\pi}{4}\right)^3 k_I^6\, \frac{1-\nu}{\mu}\, \frac{(T_{YY})^2}{P}$$
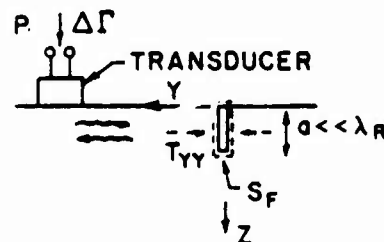
FIGURE 12

Eddy current versus ultrasonic inversion of "small" semicircular surface cracks.

VI. OPERATING FREQUENCY OPTIMIZATION

Figure 9 illustrated the principle of phase discrimination, in which the trajectory of the liftoff signal in the complex impedance plain is oriented along the horizontal (or I) channel of the display tube and the flaw signal is read from the vertical (or Q) channel. The modeling theory summarized in the preceding sections, and detailed in the references, predicts the frequency dependence of both the flaw and liftoff signals. From this it is possible to predict the frequency required for optimizing the flaw/liftoff ratio. If the ratio is taken between the flaw signal S and the total liftoff signal (in the

12

TWO-DIMENSIONAL CRACK - UNIFORM FIELD

### LARGE a/δ

$$\Delta Z_u = \frac{(h^I)^2}{\sigma I^2} \left\{ \underbrace{2(1+i)\frac{a}{\delta}}_{①} \underbrace{-1.56}_{②} + \underbrace{i\frac{A_F}{\delta^2}}_{③} \underbrace{-(1+i)\frac{\Delta u}{\delta}}_{④} \right\}$$
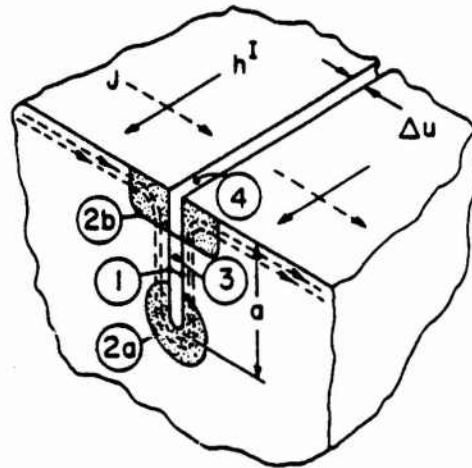
①   WALL EFFECT - SURFACE IMPEDANCE

②a, ②b   KANN EFFECT - RANGE ≈ δ

③   FARADAY EFFECT - CRACK OPENING INDUCTANCE
          - A_F = OPENING AREA

④   UNPERTURBED SURFACE IMPEDANCE

FIGURE 13

Two-dimensional surface crack in a uniform field.

horizontal channel of Fig. 9), the frequency dependence is as shown schematically in the lower curve of Fig. 15. On the other hand, if the ratio is taken with the residual liftoff N in the vertical channnel of the display tube the upper curve of the figure is obtained. This is a significant difference because it predicts that, without liftoff phase discrimination, the optimum frequency is at $a/\delta = 1$, while the optimum with phase

13
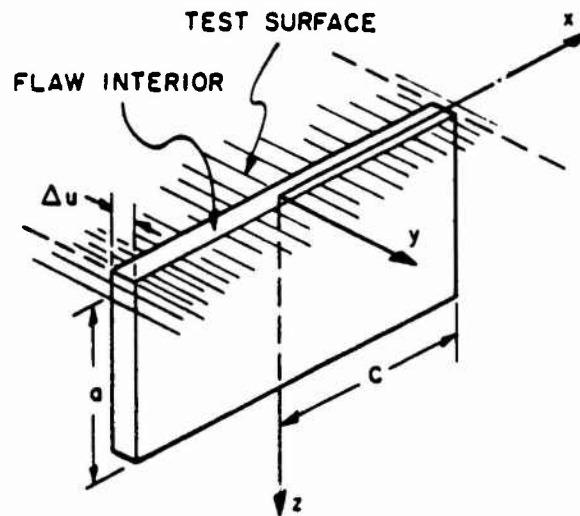
FIGURE 14

A three-dimensional rectangular surface crack.
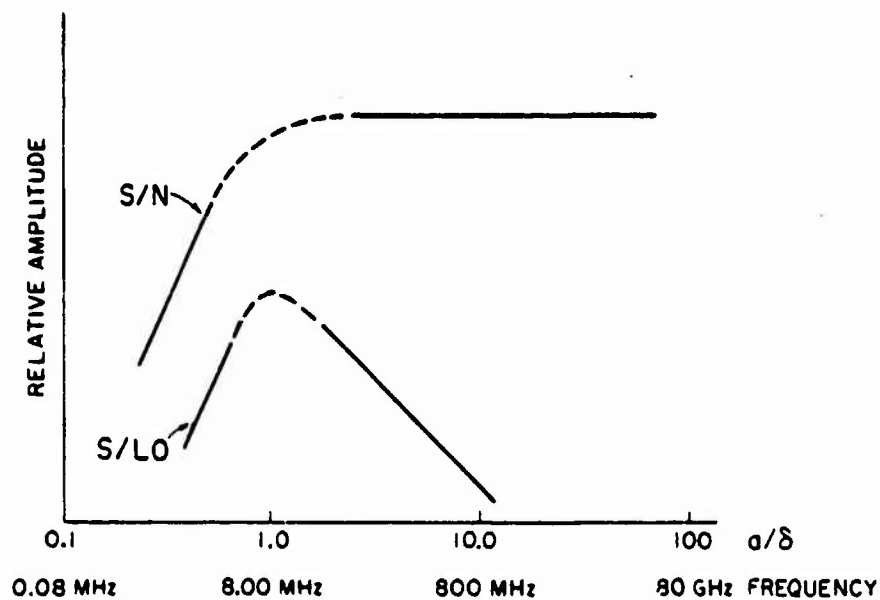
FIGURE 15

Ratio of flaw-to-liftoff as a function of frequency.

14

discrimination is for $a/\delta > 1$. To illustrate the practical significance of this result, actual frequencies are shown on the horizontal axis of Fig. 15 for a crack with a equal to 0.2 mm in stainless steel.

VII. UNIFORM FIELD VERSUS NONUNIFORM FIELD DETECTION

Figure 7 showed how the nonuniformity of the field interrogating a flaw depends on the geometry of the probe. For a given probe it also depends on the size of the flaw relative to the probe. This is illustrated in Fig. 16. The left side of the figure shows a large flaw and a small flaw superposed on a plane view of the eddy currents induced by a simple absolute coil (Fig. 2). On the right of the figure is given the variation of the z component of the applied magnetic field along the x axis. This is the interrogating field, since the y component of the magnetic field is zero in the plane of the flaws postioned as shown. The large flaw at the center of the coil is interrogated by a highly nonuniform field, as was noted in connection with Fig. 2. By contrast, the small flaw positioned at the maximum value of H_z is in an almost uniform field. This is the ideal position for application of the uniform field theory described above, but it is not one frequently encountered in practice. For this reason it has been necessary to extend the theory to the case of a nonuniform interrogating field.[6] No change in principle was involved; only a modification of the equations and the software was required. Detailed calculations have been made for approximately rectangular shaped EDM notches of dimensions such that the interrogating field of the probe used in the experimental tests was substantially nonuniform over the length of the flaw. These calculations were made for different postions of the flaw relative to the probe. A comparison of theory and experiment is shown in Fig. 17 for different values of a/δ, with X_0 denoting the distance of the center of the flaw from the center of the coil.[6,7]

VIII. FLAW SIGNAL INVERSION IN A UNIFORM FIELD

Figure 17 showed good agreement of theory and experiment for nonuniform interrogating fields at values of a/δ as small as 1.5. It is not immediately clear how to use these results for inverting the signal data to determine the characteristics of the flaw. (Since the original presentation of this paper, an approach to the general inversion problem has been developed and is presented in Ref. 8). The problem of the uniform interrogating field is much simpler and can be approached algebraically. Figure 18 illustrates the method. The ΔZ formula for a rectangular surface crack in a uniform field can be reduced to the form shown in the figure, where the crack dimensions are defined in Fig. 14, δ is the skin depth, and ΔZ is normalized by the constant interrogating field factor of Eq. (2). Inversion proceeds by the following steps:[5]

(a) The Σ's are functions of a/c only.

(b) The frequency appears in δ only.

(c) The expression in curly brackets is a polynomial $1/\delta$ in unknown coefficients.

(d) Measure ΔZ at three different frequencies.

(e) Step three gives three linear equations in the unknown coefficients of the polynomial terms. Solve for these coefficients.

(f) From the formula, the ratio of the second and third coefficients is δu, the opening of the flaw (Fig. 14).
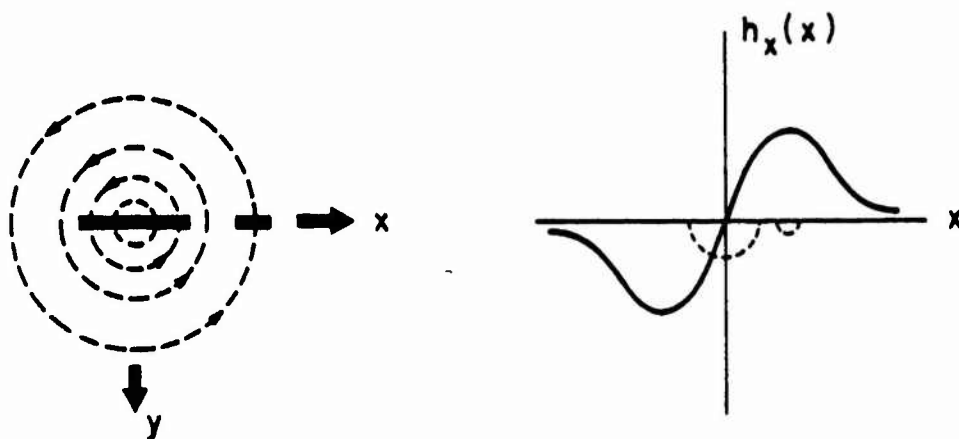
15

FIGURE 16

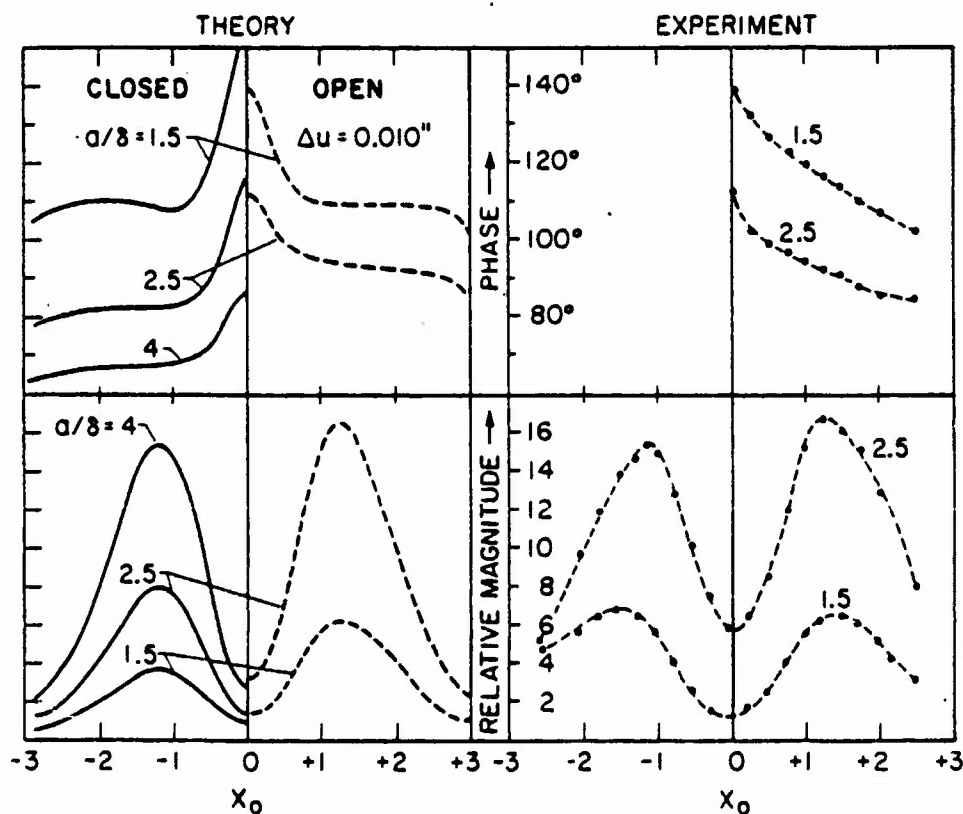Flaw detection in a uniform and a nonuniform eddy current field.

FIGURE 17

Comparison of experiment and theory for detection of a rectangular surface flaw in a nonuniform field.

(g) The square of the first coefficient divided by the second is a function of a/c only. The value of a/c can be extracted by using a lookup table constructed from Fig. 18. Value of c can then be obtained by dividing the second coefficient by Σ^1 and taking the square root.

(h) Finally, a is found as the product of c by a/c.

This procedure has not been tested experimentally because of the difficulty of realizing good uniform field conditions.

IX. PROBE FIELD MEASUREMENT

The importance to quantitative inversion of eddy current flaw signals of having an accurately measured probe field shape is clear from the above discussion. Figure 19 shows two experimental methods that have been tried for this purpose.[9] Neither of these approaches is completely satisfactory, and further research is required in this area. The Hall probe technique is restricted to frequencies lower than those used for many types of probes, and frequency scaling is possible only for air-core coils. Furthermore, the geometry of the Hall probe makes it unsuitable for very close-in measurements of the tangential (or horizontal) component of the magnetic field (Eq. 2). The perturbation technique shown at the right of the figure is satisfactory with regard to these features, but it does not give an absolute measure of the field nor is it applicable to measuring the field distribution of the probe in air. Measurement of the probe field in air is important because, as noted in Section III, the probe field over the surface of a workpiece depends on the properties of the material. The probe itself is characterized by its field in air. Once this has been measured, the field over any workpiece surface can be calculated by Fourier transform methods.

X. CONCLUSION

In this paper a review has been given of the principles involved in optimizing eddy current probes for sensitive detection and quantitative sizing of flaws, especially surface fatigue cracks. Reference 10 may be consulted for a more detailed treatment. A theoretical method was described for prediction of probe performance from knowledge of the probe field shape in air, and comparison of theory and experiment was reported for a rectangular surface flaw interrogated by a nonuniform field. There is now a need to extend these results to flaw and probe geometries that represent more realistically the practical problems encountered in the field. Examples of directions in which to proceed are: semi-elliptical surface flaws, ferrite-core coils, differential- and reflection-type probe geometries, and flaws in complicated environments such as corners and edges. Improvements are also needed in methods for measuring the fields of absolute, differential, and reflection probes. Another area requiring attention is calibration of the electronics so that the absolute magnitude and phase of ΔZ can be measured. This information is required for quantitative inversion of flaw data.

17

The graph shows curves labeled Σ^0 and $\frac{\Delta \mu}{\mu} \Sigma'$ plotted against ASPECT RATIO a/c (from 0.01 to 1.0), with vertical axis marked 0, 1.0, 2.0.

$$\Delta Z = 2c \left\{ \Sigma^0 + (1+i)\frac{c}{\delta}\Sigma' + i\frac{\Delta\mu}{\mu}\frac{c}{\delta}\Sigma' \right\}$$
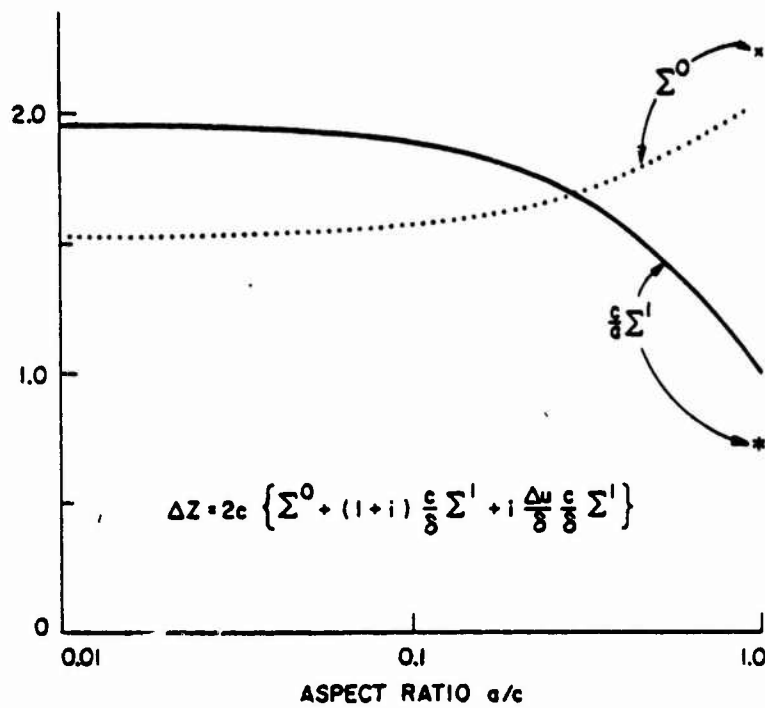
FIGURE 18

Inversion graph for detection in a uniform field.

PROBE FIELD MEASUREMENTS

SOUTHWEST RESEARCH

I

$V_H \sim H_{x,y,z}$

x

SCAN

z

HALL PROBE (1 × 4 mils)

STANFORD

$\Delta Z \sim \left(\frac{H_{tan}}{I}\right)^2$

I

SCAN

YIG SPHERE (29 mils dia.)

SMALL TEST HOLE (40 mils dia.)

FIGURE 19

Two techniques for measuring the magnetic field distribution of an eddy current probe.

REFERENCES

1. B.A. Auld and M. Riaziat, *J. Appl. Phys.* **54**, 3509 (1983).

2. B.A. Auld, in *Eddy-Current Characterization of Materials and Structures, ASTM*, **STP 722**, 332 (1981).

3. B.A. Auld, F. Muennemann, and D.K. Winslow, *J. Nondestruct. Eval.* **2**, 1 (1981).

4. B.A. Auld, F. Muennemann, and M. Riaziat, in *Proc. New Procedures in Nondestructive Testing*, ed. P. Höller (Springer-Verlag, 1983), p. 489.

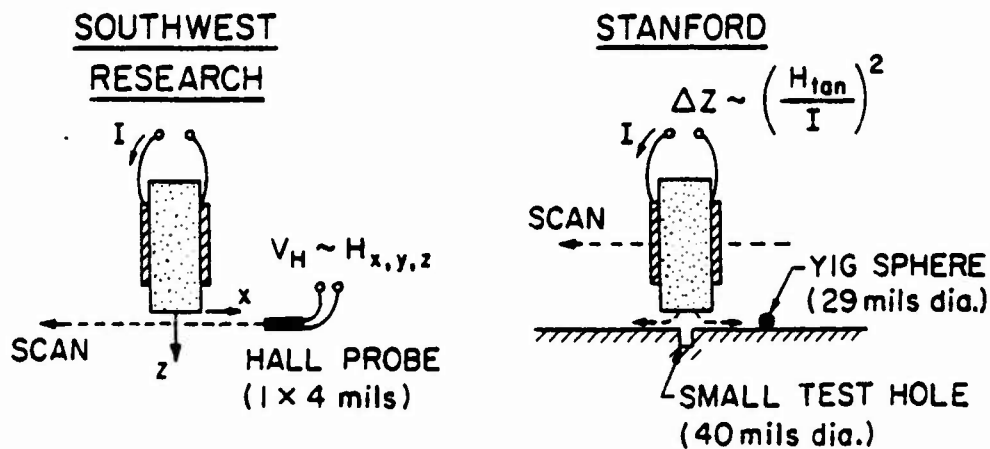5. F. Muennemann, B.A. Auld, C.M. Fortunko, and S.A. Padget, in *Review of Progress in Quantitative NDE* **2**, eds. D.O. Thompson and D.E. Chimenti, (Plenum: 1983), p. 1501.

6. B.A. Auld, S. Ayter, F. Muenneman, and M. Riaziat, in *Review of Progress in Quantitative NDE* **3**, eds. D.O. Thompson and D.E. Chimenti, (Plenum: 1984), p. 489.

7. F. Muennemann, S. Ayter, and B.A. Auld, *Review of Progress in Quantitative NDE* **3**, eds. D.O. Thompson and D.E. Chimenti, (Plenum: 1984), p. 621.

8. B.A. Auld, G. McFetridge, M. Riaziat, and S. Jefferies, to appear in *Review of Progress in Quantitative NDE* **4**, (1985).

9. B.A. Auld, F.G. Muennemann, and G.L. Burkhardt, in *Review of Progress in Quantitative NDE* **3**, eds. D.O. Thompson and D.E. Chimenti, (Plenum: 1984), p. 477.

10. B.A. Auld, F.G. Muennemann, and M. Riaziat, in *Nondestructive Testing, Vol. 7*, (Academic Press, London, 1934), p. 37.

ELASTIC WAVE INVERSE SCATTERING IN NON-DESTRUCTIVE EVALUATION

James H. Rose*
Ames Laboratory, USDOE
Iowa State University
Ames, IA   50011

ABSTRACT

Ultrasonic detection and characterization of flaws in metals and ceramics is of considerable technological interest. Scattering and inverse scattering theories have recently been applied to these tasks in a systematic manner and considerable progress has resulted. This paper first reviews briefly the development of scattering and inverse scattering methods in the AF/DARPA Program in Quantitative Non-Destructive Evaluation. Then one particular inverse method, the inverse Born approximation, is discussed in detail. Progress is reviewed and the ability of the method to distinguish volumetric and crack-like flaws is demonstrated in simple cases.

INTRODUCTION AND REVIEW

The use of high frequency sound waves to detect flaws in structural materials and machine parts has a long and varied history [1]. In particular, a strong base of engineering applications has developed in the last several decades [2,3,4]. Over the last ten years, a systematic effort has been made in the AF/DARPA Program in Quantitative Non-Destructive Evaluation to develop the fundamental scientific disciplines needed to support and extend the engineering developments [5,6].

The initial efforts in the AF/DARPA program were concerned with understanding the interaction of the probing sound beam with the flaw. Primary emphasis was placed on understanding the scattering of elastic waves by isotropic flaws in an isotropic, homogeneous elastic space. Samples were constructed with small (500μm typical dimension), well defined voids, inclusions and cracks in diffusion bonded titanium samples. Ultrasonic scattering measurements [7,8] were compared with theoretical scattering models. In particular, analytical theories were developed for the short wavelength [9], the long wavelength [10,11], and the weak scattering limits [12,13]. For the general case, numerical calculational procedures have been developed and implemented [14-19]. Agreement between theory and experiment is excellent.

Once the probe-flaw interaction was partly understood, attention was turned to the inverse-scattering method. This is the general problem of characterizing the flaw (e.g., size, shape, orientation and

composition) given the scattering amplitude. Important progress has been made in the long wavelength [10,11], the high frequency [20-22] and the weak scattering limits [23-27]. In addition, ultrasonics imaging systems based on the optical analogy methods, the high frequency asymptotic approach and the weak scattering limit can all be used to develop a single inversion algorithm [20,23,30]. This algorithm, which is the subject of this paper's main text, has been tested extensively both with experimental data [31,32] and numerically generated scattering amplitudes [33]. Again, good agreement has been obtained between theory and experiment.

Recently, the program's focus has turned to several problems which must be overcome to obtain a straightforward and cost effective implementation of the previous work in an industrial setting. First and foremost, the problem of detecting [34,35] flaws is being addressed. This effort involves the development of a measurement model which predicts the observed signal from a particular defect in a particular part [36]. Important elements in the development of a measurement model are (1) the statistics of the flaw and background distribution (2) the effects of surfaces and other boundaries and (3) the effects of diffraction and focussing on the propagation of the probing beam and the scattered signal. Important progress has been made in the development of measurement models for samples with flat and cylindrically curved surfaces immersed in water. Current efforts involve the cross-checking of the measurement model with observed signals. The good agreement obtained leads to the possibility of obtaining useful and reliable estimates of the probability of flaw detection.

In this paper we will focus on a relatively small area of progress. Namely, the development of the general inverse scattering algorithm mentioned above to determine the size, shape and orientation of internal flaws. The discussion will be developed in terms of the elastic wave inverse Born approximation (IBA) [23,24]. In Section II the derivation of the IBA is reviewed in the frequency domain. A time domain exposition is given in Section III. In Section IV we discuss a "one-dimensional" version of the IBA and test it with both theoretical and experimental data. Section V tests the full "three-dimensional" form of the IBA. Finally, the paper is concluded with a discussion and summary.

II. THE INVERSE BORN APPROXIMATION IN THE FREQUENCY DOMAIN

The direct and inverse Born approximation are reviewed in the frequency domain. Following closely the work of Gubernatis et al. [13] we describe the Born approximation for the direct scattering problem in the frequency domain. Then following Rose and Krumhansl [23] we show that it naturally leads to a simple inversion procedure.

The scattering geometry is shown in Fig. 1. A flaw with homogeneous isotropic material parameters is centered about the origin of coordinates. A plane wave in the displacement field propagates in the $+e^0$ direction and scatters off the flaw. The scattered displacement
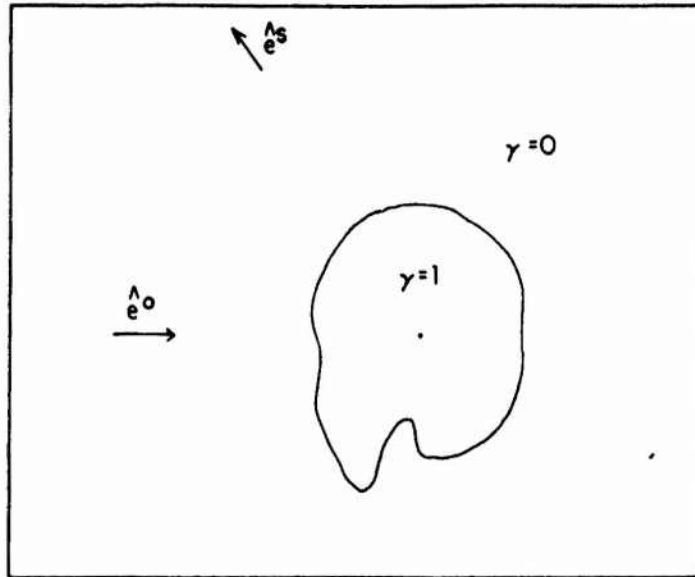
Fig. 1. Shows the scattering geometry where $\hat{e}^o$ and $\hat{e}^s$ are unit vectors in the direction of incidence and scattering, respectively. The flaw is indicated by the characteristic function, $\gamma(\vec{r})$, which is one inside the flaw and zero outside.

field is then measured in the far field in the direction denoted by $\hat{e}^s$. The polar and azimuthal angles are denoted by θ and ϕ where $\cos\theta = \hat{e}^s \cdot \hat{e}^o$. The geometric features of the flaw are described by the characteristic function $\gamma(\vec{r})$ which is one if $\vec{r}$ is inside the flaw's boundary and is zero if $\vec{r}$ is outside. The material properties of the flaw are chosen to be constant. The Lame parameters and density of the flaw are denoted by λ_f, μ_f, and ρ_f. The same quantities for the host are λ, μ and ρ. The differences in material properties are denoted by $\delta\rho = \rho_f - \rho$, $\delta\lambda = \lambda_f - \lambda$ and $\Delta\mu = \mu_f - \mu$.

The scattering process is governed by the elastodynamic wave equation which in the integral equation form [13] is

$$u_i(\vec{r},\omega) = u_i^o(\vec{r},\omega) + \omega^2 \delta\rho \int d^3r' \gamma(\vec{r}') g_{ij}(|\vec{r}-\vec{r}'|,\omega) u_j(\vec{r}',\omega) + \quad (1)$$

$$\delta C_{jklm} \int d^3\vec{r}' \gamma(\vec{r}') g_{ij,k}(|\vec{r}-\vec{r}'|,\omega) u_{l,m}(\vec{r}').$$

We use standard tensor notation. Repeated Roman indices indicate summation and commas indicate differentiation with respect to the following indices. C_{ijkl} denotes the elastic constants of the material which

are determined by the Lame parameter for an isotropic material. The displacement field is denoted by u and the incident wave is given by

$$u_i^o(\vec{r},t) = e^{ik\hat{e}^o\cdot r}\, e^{-i\omega t}\, \hat{a}_i = u_i(\vec{r},\omega)\, e^{-i\omega t} \qquad (2)$$

Here ω is the angular frequency; $\hat{a}_i$, the polarization vector; and, k, magnitude of the wave vector. The Green's function is denoted by g_{ij} and is chosen to represent out-going spherical waves. Explicitly,

$$g_{ij}(R,\omega) = \frac{1}{4\pi\rho\omega^2} \left[\frac{\delta_{ij}\,\beta^2\, e^{i\beta R}}{R} - \frac{\partial}{\partial x_i}\frac{\partial}{\partial x_j}\left(\frac{e^{i\alpha R}}{R} - \frac{e^{i\beta R}}{R} \right) \right] \qquad (3)$$

Here α and β are respectively the wavevectors of longitudinal and transverse waves and δ_{ij} is the Kronecker delta function.

For a given flaw, the solution of Eq. 1 would exactly determine the scattering problem. However, the integral equation is generally intractable and approximate solutions are often sought. The Born approximation consists of replacing the exact fields u_i and $u_{l,m}$ on the right side of Eq. 1 with the values of the incident field, i.e., u_i^o and $u_{l,m}^o$. This approximation is reasonable, if the incident wave is weakly scattered, in which case the displacement and strain fields in the flaw are nearly that of the incident wave. The far field amplitudes are given as $r \to \infty$ by

$$u_i = \left[\frac{e^{i\alpha r}}{r} A_i(\alpha,\hat{e}^o,\hat{e}^s) + \frac{e^{i\beta r}}{r} B_i(\beta,\hat{e}^o,\hat{e}^s) \right]. \qquad (4)$$

Here A_i and B_i are respectively the scattering amplitudes for longitudinal and transverse waves and $\hat{e}^s = \vec{r}/|\vec{r}|$.

The rest of our exposition will be given in terms of longitudinal to longitudinal (L-L) scattering, although the same results can be obtained for transverse to transverse and for mode-converted signals. The longitudinal scattering amplitude for an incident longitudinal wave in the Born approximation is

$$A_i(\alpha,\hat{e}^o,\hat{e}^s) = \frac{\alpha^2}{4\pi} \left[\frac{\delta\rho}{\rho} \cos\theta - \frac{\delta\lambda + 2\delta\mu\cos^2\theta}{\lambda + 2\mu} \right] S(\alpha,\hat{e}^o,\hat{e}^s)\, \hat{r}_i \qquad (5)$$

Here $S(\alpha,\hat{e}^o,\hat{e}^s)$ is called the shape factor and is defined as the k-space Fourier transform of the characteristic function, γ, i.e.

$$S(\alpha, \hat{e}^O, \hat{e}^S) = \int d^3\vec{r}\,' \; e^{i\alpha(\hat{e}^O - \hat{e}^S)\cdot\vec{r}\,'} \; \gamma(\vec{r}\,') \tag{6}$$

The inversion algorithm we use in this paper is based on the directly backscattered signal. In that case the scattering amplitude is given by

$$A_i(\alpha, \hat{e}^O, -\hat{e}^O) = \frac{\alpha^2}{4\pi}\left(\frac{\delta\rho}{\rho} + \frac{\delta\lambda + 2\delta\mu}{\lambda + 2\mu}\right) S(\alpha, \hat{e}^O, -\hat{e}^O)\hat{e}_i^O \tag{7}$$

Following Rose and Krumhansl [23] we rewrite Eq. 7 as

$$S(\alpha, \hat{e}^O, -\hat{e}^O) = \frac{\hat{e}_i^O \, A_i(\alpha, \hat{e}^O, -\hat{e}^O)}{\dfrac{\alpha^2}{4\pi}\left(\dfrac{\delta\rho}{\rho} + \dfrac{\delta\lambda + 2\delta\mu}{\lambda + 2\mu}\right)} \tag{8}$$

If the pulse-echo scattering amplitude is known for all frequencies and for all directions of incidence, then the shape factor S is completely defined. The characteristic function is obtained by an inverse Fourier transform of Eq. 6. We find

$$\gamma(\vec{r}) = \frac{1}{2\pi^2}\frac{1}{\left(\dfrac{\delta\rho}{\rho} + \dfrac{\delta\lambda + 2\delta\mu}{\lambda + 2\mu}\right)}\int \alpha^2 d\alpha \, d^2\hat{e}^O \; \hat{e}^{-2i\alpha\hat{e}^O\cdot\vec{r}} \; \frac{\hat{e}_i^O A_i(\alpha, \hat{e}^O, -\hat{e}^O)}{\alpha^2} \tag{9}$$

If the scattered signal does not depend on the incident direction (i.e., if the flaw has spherical symmetry) Eq. 9 can be simplified and we obtain

$$\gamma(r) = \frac{2}{\pi}\frac{1}{\left(\dfrac{\delta\rho}{\rho} + \dfrac{\delta\lambda + \delta\mu}{\lambda + 2\mu}\right)}\int d\alpha \, \frac{\sin 2\alpha r}{2\alpha r} \, \hat{e}_i \; A_i(\alpha, \hat{e}^O, -\hat{e}^O). \tag{10}$$

Equation (10) is the form of the inversion algorithm most commonly used in experimental evaluation. The determination of the characteristic function requires a knowledge of $\delta\rho$, $\delta\lambda$ and $\delta\mu$. If we are only concerned with the shape (geometric features) of the flaw it is not necessary to know the material property deviations since they only appear as an overall multiplicative factor. In the following results we will replace the prefactors in Eqs. (9) and (10) by a positive constant. Consequently, in the inversions which follow the shape of the flaw is determined but $\delta\rho$, $\delta\lambda$ and $\delta\mu$ are undetermined.

The two inversion formulas (Eqs. (9) and (10)) are valid in the weak scattering limit. Our purpose in this paper is to test how well they work for strongly scattering flaws. Because of the assumed spherical symmetry, Eq. (10) can be evaluated using only a single pulse-echo record (i.e., the amplitude for a single angle of incidence, but for all frequencies). This is an important simplification over Eq. (9) especially in some NDE applications where only a single angle of viewing is available. Equation (10) can also be used if multiple viewing angles are available to obtain a reconstruction of ellipsoidal flaws. This feature will be discussed in Section IV.

Two ambiguities arise in the inversion procedure for strongly scattering flaws. First, the shape factor is no longer uniquely and exactly related to the scattering amplitudes. One could, for example, approximate S from pitch-catch experiments (where $\hat{e}^O \neq \hat{e}^s$), as well as the more restricted pulse-echo used in eq. (8). A report on the experimental test of this possibility is contained in Ref. (32). However, in this paper, we will rely entirely on pulse-echo data. Our choice stems from the relative experimental ease of collecting these data and from the fact that the Born approximation for the direct scattering problem works best for the pulse-echo mode.

A second ambiguity arises, since A_i (which is a real function for weakly scattering flaws with a center of inversion symmetry) becomes a complex valued function for flaws with finite scattering strength. Using Eqs. (9) and (10) without modification would lead to a predicted complex value for the characteristic function, $\gamma(\vec{r})$. This is in contradiction to our original assumptions and arises when strong scattering data is used in the inversion. Empirically, it has been found that the reconstruction of volumetric flaws is found in the real part of $\gamma(\vec{r})$, while the reconstruction of crack-like flaws is found in the imaginary part of $\gamma(\vec{r})$. A reconstruction of the entire flaw is obtained by evaluating $|\gamma(\vec{r})|$.

III. TIME DOMAIN BORN INVERSION ALGORITHM

The time domain picture proves useful in explaining how the Born inversion procedure can yield accurate results for the size, shape and orientation of strongly scattered volume flaws. We follow Rose and Richardson [26] in describing the direct and inverse scattering problems. We will further indicate how the algorithm can be reduced to a practical form for strongly scattering flaws. Finally, we discuss in a schematic way the inversion procedure for a strongly scattering spherical void.

The scattering geometry for the time domain is much the same as for the frequency domain. An incident delta function plane wave displacement field impulse propagates in the $+e^O$ direction and is given by

$$u_i^o(\vec{r},t') = u_i^o \, \delta(t'-\hat{e}^O \cdot \vec{r}/c) \qquad (11)$$

Here c is the longitudinal velocity of sound in the host. We note that the impulse is chosen to cross the origin of coordinates which is centered in the flaw at $t' = 0$.

The form of the scattered displacement field in the Born approximation .can be determined either by iterating a time domain integral equation analogous to Eq. (1) or by Fourier transforming the scattering amplitude as given in Eq. (5) to the time domain. The scattered displacement field at an observation point r' and a time t' is given for large $|\vec{r}'|$ as

$$u_i^s(\vec{r}',t') = \lim_{|\vec{r}'| \to \infty} \frac{1}{|r'|} R_i(\hat{e}^o,\hat{e}^s,t'-r'/c) \tag{12}$$

R_i (defined by this equation) is called the impulse response function. It is related to the frequency domain scattering amplitude by

$$R_i(\hat{e}^o,\hat{e}^s,t) = \frac{1}{2\pi} \int_{-\infty}^{\infty} e^{-i\omega t} A_i(\omega,\hat{e}^o,\hat{e}^s) \, d\omega. \tag{13}$$

Here $t = t'-r'/c$ and ω is the angular frequency, $\omega = c\alpha$. Within the Born approximation R_i is

$$R_i(\hat{e}^o,\hat{e}^s,t) = f(\hat{e}^o \cdot \hat{e}^s)e_i^s \frac{d^2}{dt^2} \int d^3r' \gamma(\vec{r}') \, \delta(t - \frac{(\hat{e}^o - \hat{e}^s) \cdot \vec{r}'}{c}). \tag{14}$$

The function $f(\hat{e}^o \cdot \hat{e}^s)$ is a geometrical factor involving the material property deviations and is given emplicitly by

$$f(\hat{e}^o \cdot \hat{e}^s) = \frac{\delta\rho}{\rho} \cos\theta - \frac{\delta\lambda + 2\delta\mu \cos^2\theta}{\lambda + 2\mu} \tag{15}$$

Here $\cos\theta = \hat{e}^o \cdot \hat{e}^s$. The integral in Eq. (14) has an interesting interpretation. It is the cross-sectional area of the flaw intersected on a plane defined by $t = (\hat{e}^o - \hat{e}^s) \cdot \vec{r}/c$. The straightforward and intuitively appealing use of Eq. (14) to determine impulse response functions is discussed for several simply shaped flaws in Ref. 26.

In order to define the inversion procedure we consider the L-L pulse-echo response function, $R(\hat{e}^o,-\hat{e}^o,t)$, for all directions of incidence $\hat{e}^o$. Since the impulse response function defines the projection of $\gamma(\vec{r})$ onto planes, the characteristic function can be obtained

from the Radon transform. A discussion of the connection between the Radon transform and the inverse Born approximation is given in Refs. (37) and (38). The resulting inversion formula is

$$\gamma(\vec{r}) = \text{const.} \int d^2\hat{e}^o \; \hat{e}^o_i R_i(\hat{e}^o, -\hat{e}^o, \; t = 2\hat{e}^o \cdot \vec{r}/c) \tag{16}$$

This equation can be verified directly by substituting Eq. (13) in (16). Equation (16) simplifies for the case of spherical symmetry and one obtains

$$\gamma(r) = \text{const.} \; \frac{1}{(2r/c)} \int_{-2r/c}^{2r/c} \hat{e}^o_i R_i(\hat{e}^o, -\hat{e}^o, t) dt \tag{17}$$

In order to illustrate the use of the time domain inversion procedure, we consider a spherical flaw in the weak scattering limit. The Born approximation for the time domain impulse response is shown in Fig. 2A. The inversion procedure averages the impulse response function from -2r/c to 2r/c in order to determine the value of the characteristic function at point r. The result is shown in Fig. 2B. The characteristic function drops abruptly to zero when the average includes the delta functions which occur at -2a/c and 2a/c (here a is the radius of the sphere). We will return shortly to a consideration of the inversion procedure for a strongly scattering spherical flaw. First, however, we must deal with the ambiguities in producing an algorithm from the formalism which were mentioned in the last section.

In order to evaluate Eqs. (16) or (17), it is necessary to know the zero of time about which the average is to be performed. This turns out to be one of the greatest difficulties in inverting experimental data. Formally, the zero of time to be used by Eq. (12) is defined by $t = t'-r'/c = 0$. An interpretation of this definition is to imagine launching a spherical longitudinal wave, from the origin of coordinates at time $t' = 0$, which travels with the velocity of the host. Physical events at the point of observation are then measured with respect to the arrival of this wave front. However, this definition, based on an absolute arrival time, is not directly usable experimentally, since the distance from the center of the flaw to the observation point, $|r'|$, is not available. For flaws with a center of inversion symmetry (with which we are primarily concerned) this difficulty has an elegant solution [39]. Reverting to the frequency domain for a moment, we note that for small frequencies the scattering amplitude can be expanded as

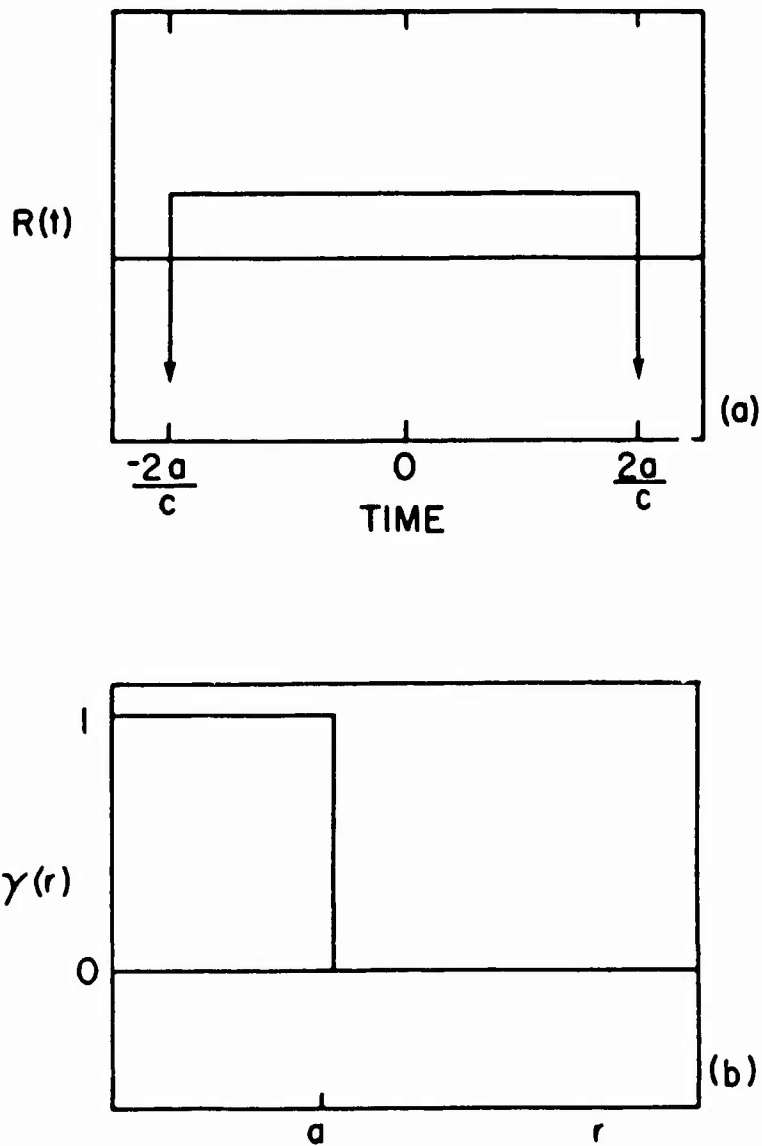$$A(\omega) = a_2\omega^2 + ia_3\omega^3 + a_4\omega^4 + ia_5\omega^5 + \dots \tag{18}$$

Fig. 2. a) The backscattered impulse response function calculated in
the Born approximation for scattering from a spherical flaw.
b) The reconstructed characteristic function corresponding
to the impulse response in Fig. (2a).

It has been shown by Richardson [40] that if the flaw has a center of inversion symmetry and if the phase shifts are calculated with respect to this center, then $a_3 = 0$. That is, the imaginary part of the amplitude rises as ω^5 for small ω. This condition fixes the zero of time in the following way. Suppose we are given an impulse response, R_i, but with an arbitrary zero of time. This is the common experimental situation. Then we can pick some zero of time and Fourier transform R_i to obtain the scattering amplitude. Only for the correctly chosen zero of time will the coefficient of ω^3, a_3, vanish. If there is an error, Δt, in the choice of the zero of time then $a_3 = a_2\omega\Delta t$. For spherical voids of radius 'a' in Si_3N_4 and Ti alloy, a realistic use of Eq. (18) to fix the zero of time requires values of the scattering amplitude for $\alpha a < .5$. The proper choice of the zero of time leads unambiguously to a determination of the real and imaginary parts of the scattering amplitude.

For a strongly scattering spherical flaw the inversion procedure has some interesting features. Figure 3A shows a schematic impulse response function. The most prominent feature of the impulse response is a large delta-function specular reflection occurring at time $t = -2a/c$. The much smaller later arriving signal is the result of the creep waves which propagate around the 'dark' side of the sphere. When Eq. (17) is used to invert an impulse response function of this form, the characteristic function, shown schematically in Fig. 3B, is found. The most striking feature of this characteristic function is the large discontinuity in γ which occurs at the actual radius and this allows an exact determination of the flaw's size. Rose and Opsal [27] have used the general time domain results to show that the size, shape and orientation of a convex void can be determined exactly from the inverse Born approximation given exact L-L backscattered data for all time and all direction of incidence. The empirical results to be discussed in the rest of the paper completely support these conclusions.

IV. ONE DIMENSIONAL BORN INVERSION

A. Theoretical Results

In this section we will test the ability of the algorithm to size spherical flaws in an isotropic and otherwise homogeneous elastic medium. The elastic wave equation is separable in spherical geometries. Consequently, a series solution can be obtained for the scattering amplitude of a homogeneous spherical flaw. This series solution, first introduced by Ying and Truell [41], was used to determine the scattering for two sets of flaws [42]. First the backscattered amplitude was determined for spherical voids of radius a in various materials. Equation (10) was used to evaluate the characteristic functions which are plotted in Fig. (4). We note that in all cases, the characteristic function is large inside the nominal radius of the flaw and drops abruptly to zero at the correct radius. The numerical data was calculated $.1 < \alpha a < 10$, where a is the nominal radius of the flaw, in steps of 0.1. The cutoff in data at $\alpha a = 10$ leads to the rounding of the characteristic function near the nominal radius and to the oscillations in the reconstruction (Gibb's phenomena).
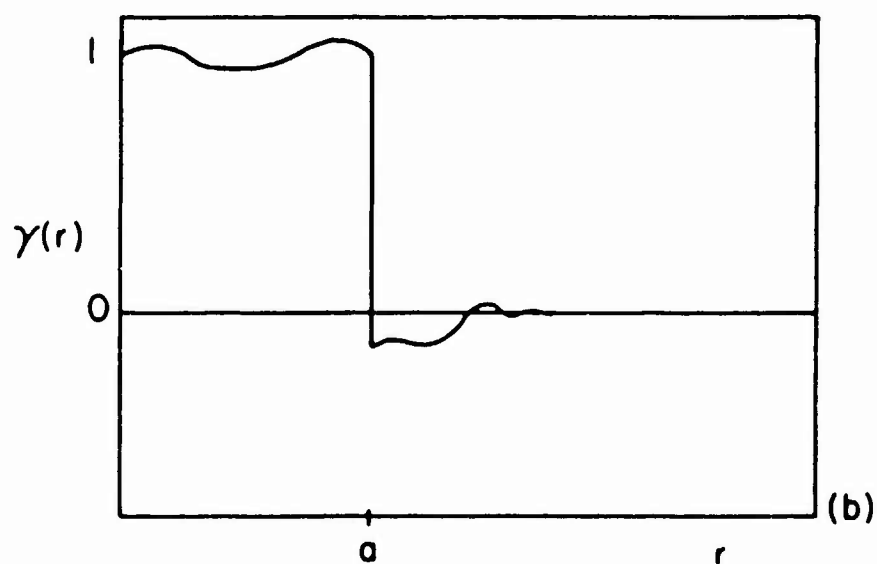
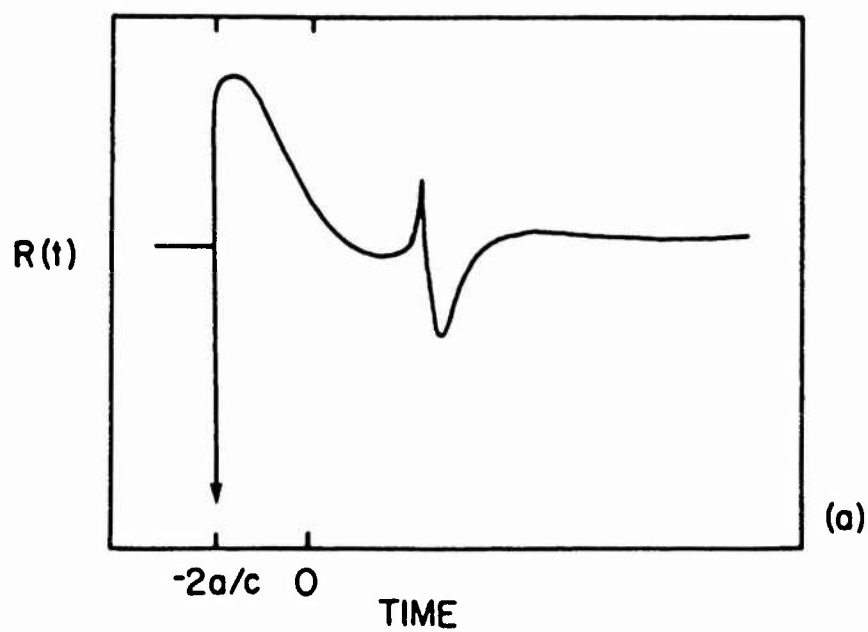Fig. 3. a) Schematic representation of the true impulse backscattered
response function for a spherical void in a metal. b) A sche-
matic characteristic function corresponding to the impulse
response in Fig. (3a).
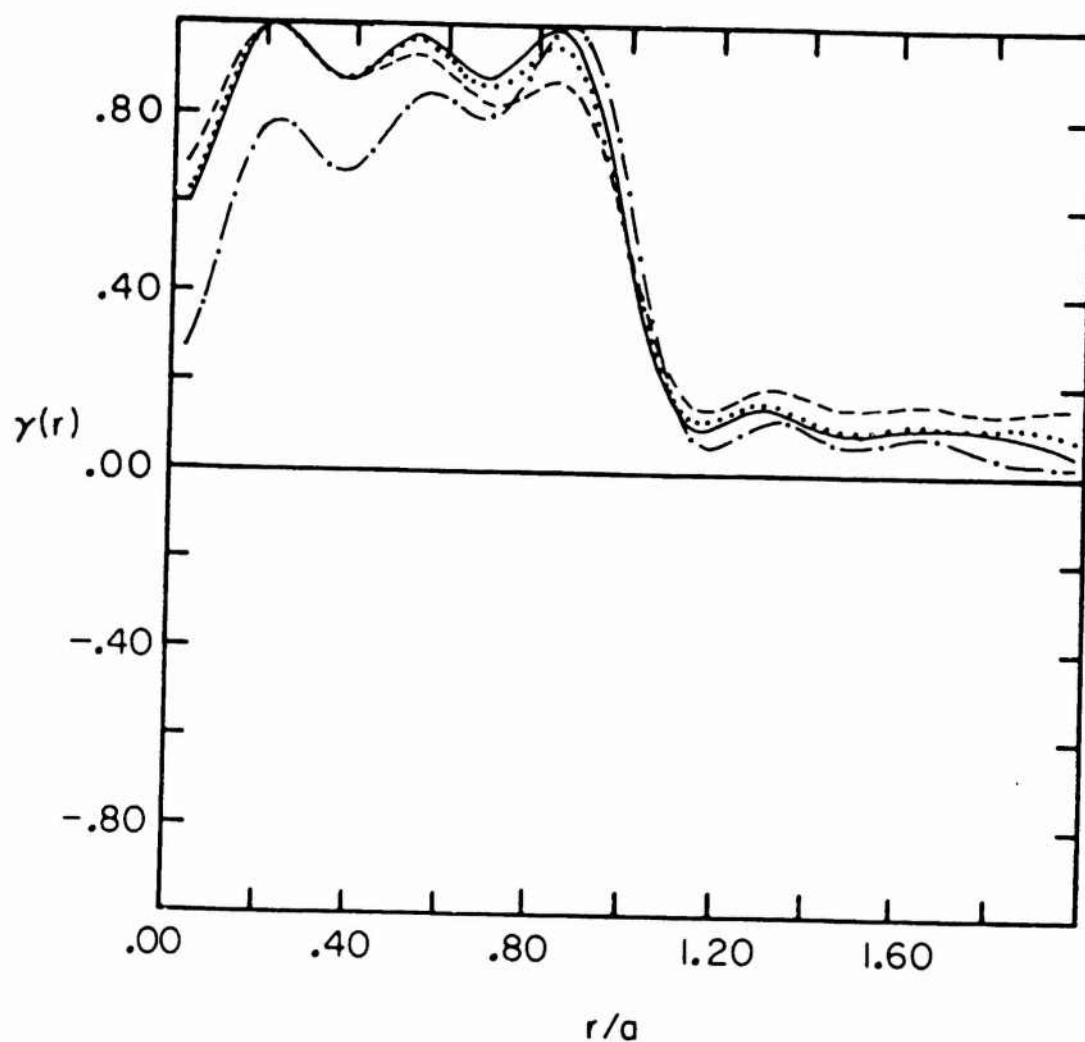
Fig. 4. Calculated characteristic functions, using Eq. (10) with back-
scattered longitudinal waves, .10<αa<10, for spherical voids
in various solids Ti and Al ___, Brass..., Tungsten carbide
- · - and Pb --.
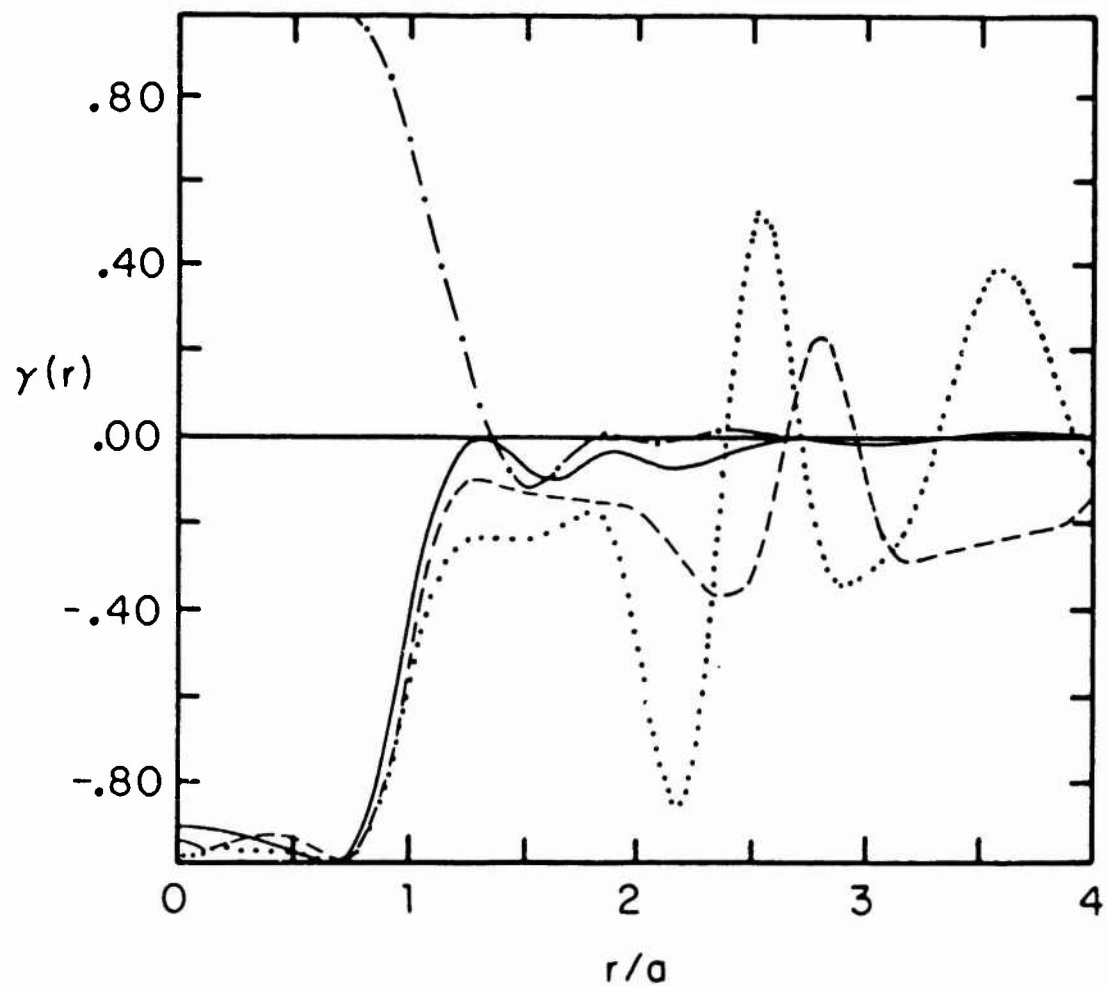
Fig. 5. Calculated characteristic functions, using Eq. (10) with back-
scattered longitudinal waves, $.10 < \alpha a < 10$, for spherical inclu-
sions: silicon inclusion in silicon nitride, $Si:Si_3N_4$ - - -;
$Fe:Si_3N_4$ .....; $W:Si_3N_4$ --- and a tungsten carbide inclusion
in titanium ___. The first part of the characteristic function
$(R \rightarrow 0)$ is positive if the impedance of the flaw is less than
that of the host.

Scattering amplitudes were also calculated for a series of inclusions in Si_3N_4. Results are shown in Fig. (5). These results are quite different from those obtained for voids. First of all, the estimated characteristic function is, in most cases, negative. This results since the acoustic impedance of the flaw is greater than that of the host. Upright characteristic functions are obtained when the acoustic impedance is less than the host (see the comment following Eq. (10)). All of the reconstructed characteristic functions drop abruptly to zero at the nominal radius. However, spurious features may occur at larger values of r. See, for example, the result of the iron (Fe) inclusion. These spurious features result from multiple scattering of the incident beam within the inclusion. They present a significant difficulty when present (although see Hsu et al. (32)). Fortunately, the occurrence of such substantial effects is unusual for many of the realistic inclusions found in metals.

B. Experimental Results

The experimental validation of the "one-dimensional" form of the IBA has been carried out by several groups [31,32]. Figure (6) shows the reconstructed characteristic function for a 400μm radius spherical void in a diffusion bonded titanium sample [43]. The data was taken by R. K. Elsley for backscatter and 0.5<αa<4.0, where a is the radius of the flaw. The inferred characteristic function, γ, is rounded due to the lack of high frequencies. Even so, a relatively accurate estimate is obtained for the radius by finding the value of r for which γ is half of its maximum value. These results are typical. The estimated radius agrees with the nominal radius of the flaw to within 10%.

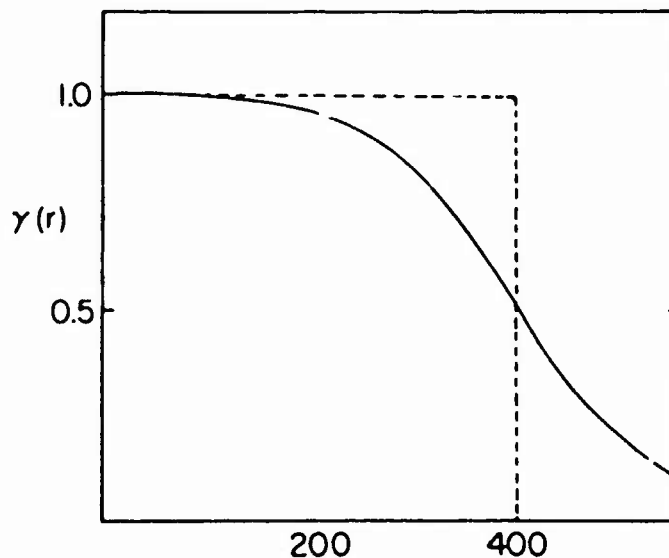Fig. 6. Reconstructed characteristic function for a 400μm spherical void in a titanium sample. The backscattered longitudinal to longitudinal signal was measured for .50<αa<4.0 and used to obtain γ($\vec{r}$) via Eq. (10).

Perhaps the most systematic examination of the experimental inversion of spherical flaws was carried out by Elsley and Addison [31]. They measured scattering amplitudes for a wide variety of spherically symmetric flaws both in titanium and in Si_3N_4. Their results are reported in Table 1. As can be seen, good reconstructions were obtained if the scattering amplitude was experimentally accessible for $.5 < \alpha a < 2.5$. They further verified this observation by considering exact solutions from the Ying-Truell solutions for a spherical void in titanium and truncating both the minimum and maximum values of αa included in the inversion algorithm. The inversion remains relatively accurate as high frequencies are removed as long as $\alpha a_{max} > 2$. For $\alpha a_{max} < 2$, the method becomes diffraction limited and overestimates the size of the flaw. As low frequencies are removed, the method tends to systematically underestimate the size of the flaw.

More recently, Hsu et al. have investigated the use of the one-dimensional algorithms in a variety of circumstances. It was shown to be useful for flaws near a water-solid interface [44], for certain flaws with large resonant scattering amplitudes and for pitch-catch (bistatic) measurements.

It was suggested in Ref. (45) that the "one-dimensional" IBA could be used to determine the shape of an ellipsoidal flaw if backscattered data were available for several directions of incidence. Hsu et al. [44] implemented this idea and accurately determined the size, shape and orientation of spheroidal voids and inclusions in elastic materials.

V. "THREE-DIMENSIONAL" BORN INVERSION

A. Theoretical Results

The calculation of elastic wave scattering amplitudes for isolated, non-spherically symmetric flaws is rather difficult. Most methods obtain a solution by expanding the field, $u_i(\vec{r},\omega)$, in terms of a basis set. In one method the boundary conditions are satisfied variationally [15,16]. The result is a matrix equation for the expansion coefficient which when solved numerically determines the scattered field. With the largest computers, most solutions have been restricted to axially symmetric flaws since this substantially simplifies the solution of the matrix equation.

Rose and Opsal [35] have reported the inversion of several of these numerically "exact" scattering amplitudes for a variety of axially symmetric voids and cracks. The backscattered amplitudes were calculated, using the method of optimal truncation [19], for $0.1 < \alpha a < 10$ and for five degree increments of the polar angle. The characteristic function was evaluated using Eq. (9). Since the flaw is assumed to be axially symmetric the integration over the azimuthal angle was carried out analytically.

Figure 7(a) shows the reconstruction of an edge-on penny shaped crack. The solid line shows the boundary of the crack. The dashed

Table 1. From Ref. (31). Shows estimated radii of various flaws in a titanium alloy (Ti-6Al-4V) and in a ceramic material (Si₃N₄). The first column defines the flaw, the second column gives a measure of signal-to-noise while the third and fourth columns define the smallest and largest values of αa for the measured signal. Columns five and six contain the true and estimated radii, respectively.

Flaws in Ti-6Al-4V

Flaw	S/N(dB)	αa_{min}	αa_{max}	True Radius (μm)	Estimated Radius (μm)	Comments
1. Void Sphere	10	.2	3	400	388	0° Incidence
					398±4	
					402±4	
2. Void Prolate 415 x 806μm	-10	.5	2.5	415	443	
3. Void Sphere	20	.5	3	400	374	
4. WC Sphere	10	.5	3	400	325	
5. Void Sphere	-13	.6	2.5	400	347	
6. Void Sphere	10	1.2	4.2	600	361	No low ka
7. Void Oblate 390 x 130μm	-10	.6	1.1	225	330	No high ka

Flaws in Si₃N₄

Flaw	S/N(dB)	αa_{min}	αa_{max}	True Radius (μm)	Estimated Radius (μm)	Comments
1. Fe Sphere	25	.5	4	200	190	
2. Si "Sphere"	10	.5	3	"50"	38	Highly Distorted
3. Void "Sphere"	10	1.0	5.5	250	180	No low ka
4. Void "Sphere"	0	.5	2.8	125	132	

line is the 50% equal value contour of the characteristic function. Figures (7b-d) show similar results for: (7b) a spherical void intersected by a flat circumferential crack; (7c) a spherical void with a second spherical void half its radius appended; and (7d) a spherical void with an attached capped cylindrical void (the 40, 50 and 60% contours are shown). In all cases, the algorithm was successful in reconstructing the flaws. Thus it was shown that the method (1) can be applied to cracks (2) can deal with flaws with hollows and (3) can deal with sharp corners in the shape of the flaw. Perhaps the inversion of the composite flaw (void and crack) in Fig. 7b is the most important result, since this shows that the same algorithm can be used to treat both types of defects.
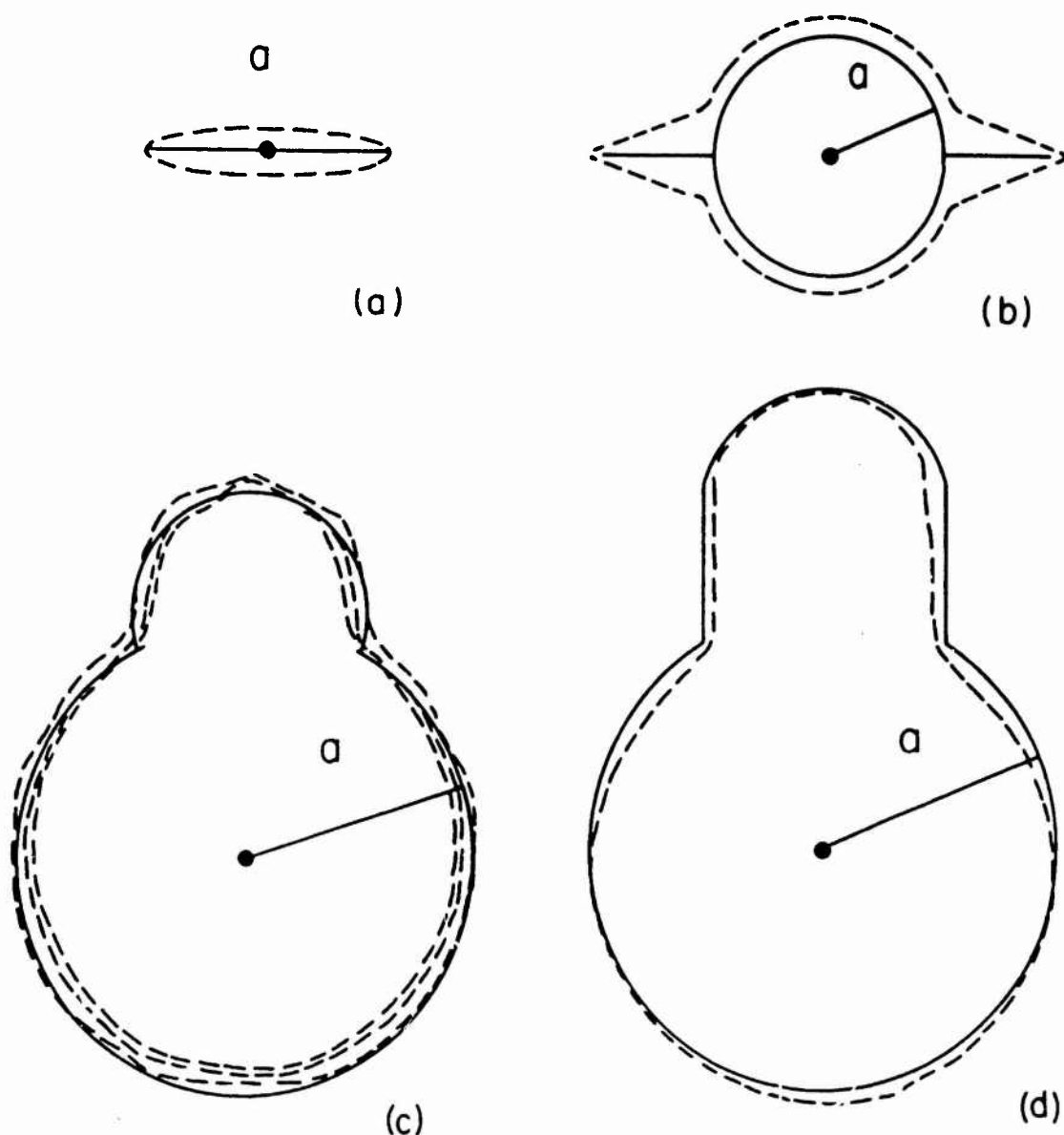
Fig. 7. Reconstructions of various flaws using the "three-dimensional"
Born inversion algorithm defined by Eq. (9). All the flaws
are axially symmetric and L-L backscattered amplitude were
calculated for .10<αa<10 and for five degree increments of
the polar angle. The solid lines show the nominal shape of
the flaw while the --- line shows the 50% equal value contour
of the characteristic function $\gamma(r)$. (7a) Reconstructed char-
acteristic function for a penny-shaped crack lying edge-on,
(7b) Reconstructed characteristic function for a spherical
void with a circumferential flat crack lying edge-on, (7c)
Reconstructed characteristic function for a flaw consisting
of a spherical void with a smaller spherical void appended.
Here we show the 40, 50 and 60% equal value contours. (7d)
Reconstructed characteristic function for a spherical void
with a capped cylinder appended.

Recently the inversion of the "Saturn ring" flaw has been repeated. Figure 8a shows a plot of the real part of the characteristic function, while Fig. 8b shows the imaginary part. Finally, Fig. 8c shows the magnitude. The values plotted represent the 70% contour of $\gamma(\vec{r})$. As can be seen, it is possible in this way to cleanly separate the volumetric from the crack-like portions of the flaw. The ability to distinguish cracks from voids and inclusions is important. The presence of a crack in a part is likely to be dangerous while, for example, some inclusions are entirely benign.

B. Experimental Results

Experimental tests of the "three-dimensional" form of the IBA (Eq. (9)) are quite recent and generally unpublished. Elsley [46] has presented preliminary results for the reconstruction of $\gamma(r)$ for a 200-400μm oblate spheroid. He found that the algorithm accurately determined the size of the flaw. However, the shape of the flaw was distorted. apparently due to certain artifacts in the integration scheme. Later Rose [47] et al. inverted the same data for the oblate spheroid and similar data for a 200-400μm "Saturn ring" flaw. The sizes and shapes of these flaws were accurately reproduced including the cracked region of the "Saturn ring" flaw. Full details will be published elsewhere.

VI. DISCUSSION

The inverse Born approximation has been shown to be an appropriate means of characterizing certain isolated flaws in metals and ceramics. In particular, it is possible to determine the size, shape and orientation of the flaw given adequate experimental data. The primary experimental concern is to measure the backscattered amplitude for a sufficiently broad bandwidth and over a sufficiently wide apreture. The method appears to work equally well for volumetric flaws (voids and inclusions) and for cracks. Further, the examination of the real and imaginary parts of the characteristic function provides a method for distinguishing voids and cracks, even when they are part of the same flaw.

The agreement between theory and experiment are surprising given the bases of the theory. However, as we remarked in the introduction the same algorithm can be derived on other grounds in the high frequency limit for voids [20]. Additionally, the inversion algorithm is very similar to that used in acoustic backscatter tomography. The fact that these diverse "single-scattering" approaches yielded the same method supports the wide range of validity found empirically. References (27) and (30) discuss in some further detail the reasons for the IBA's success and its connection to the synthetic aperture imaging method.

In this paper the determination of the flaw's geometric features were discussed. The material properties of the flaw were ignored. This arises in large part from the fact that only recently have
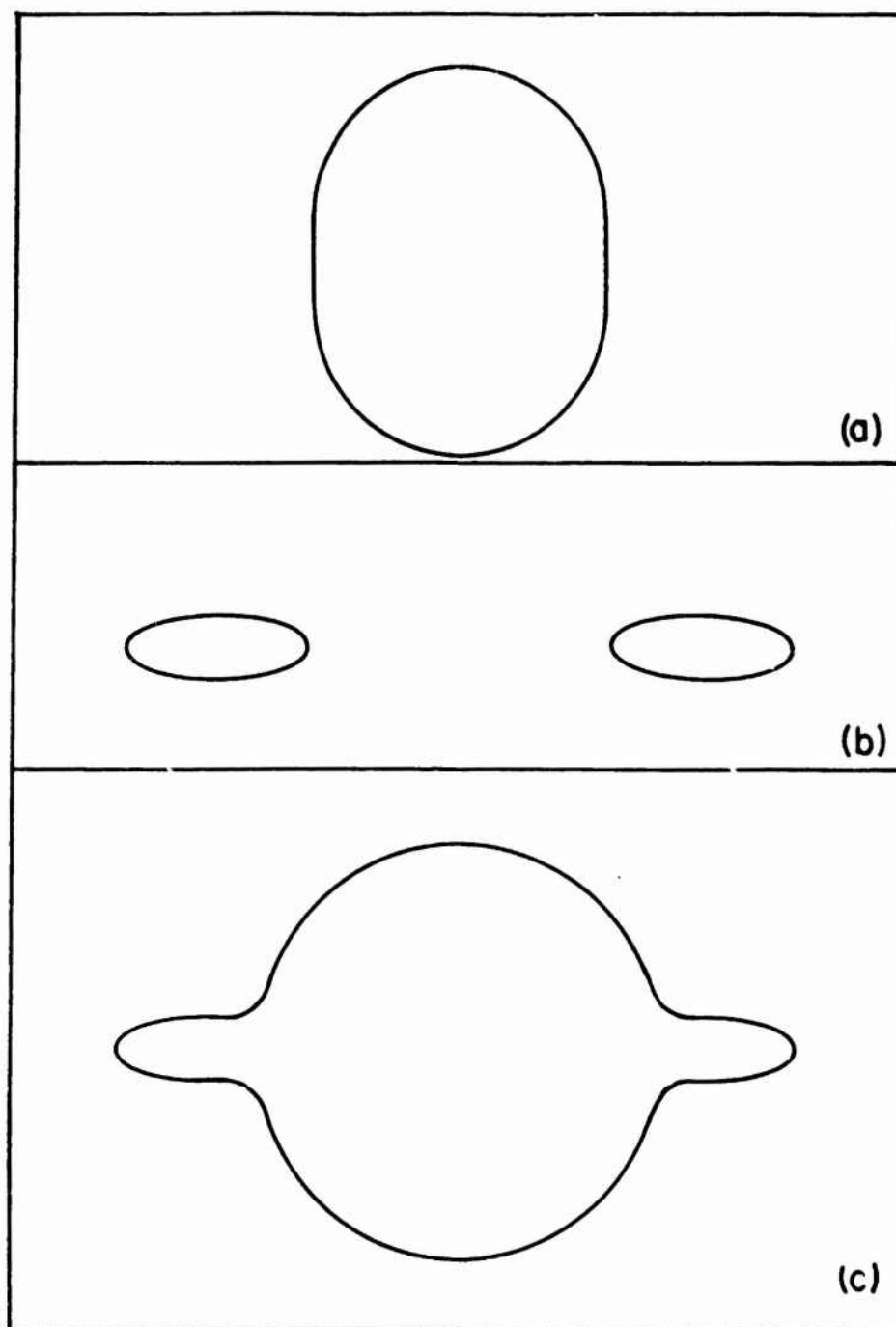
Fig. 8. Reconstructed characteristic function $\gamma(\vec{r})$, for a "Saturn ring" flaw. (8a) real part of reconstructed characteristic function. (8b) Imaginary part of reconstructed characteristic function. (8c) Magnitude of reconstructed characteristic function.

absolute (as opposed to relative) measurements of the scattering am-
plitude become routinely available. A considerable amount of future
work involves using these absolute measured amplitudes to 1) develop
corrections to the IBA's predictions of the geometric shape and 2) to
predict the material properties of the flaw.

In summary, the inverse Born approximation has been shown to be
a simple and direct way of inverting ultrasonic scattering amplitudes
to find the geometric features of isolated flaws in the bulk of a
structural material.

REFERENCES

1. See, for example, the Proceedings of the IEEE Symposium on Sonics
   and Ultrasonics.
2. See, for example, the Journal of Nondestructive Evaluation.
3. See, for example, Materials Evaluation, the Journal of the
   American Society for Nondestructive Testing.
4. J. Krautkramer and H. Krautkramer, Ultrasonic Testing of Materials,
   (Springer-Verlag, Berlin, 1977).
5. Review of Progress in Quantitative NDE 1, D. O. Thompson and D.
   E. Chimenti, Eds., (Plenum Press, New York, 1982).
6. Review of Progress in Quantitative NDE 2, D. O. Thompson and D.
   E. Chimenti, Eds., (Plenum Press, New York, 1983).
7. B. R. Tittmann, R. Elsley and N. Paton, "Measurements of ultra-
   sonic scattering from bulk flaws of complex shape", in Proceed-
   ings of the DARPA AFML Review of Progress in Quantitative NDE,
   report AFWAL-TR-80-4078 (Air Force Wright Aeronautical Labora-
   tories, Dayton, 1979), pp. 359-365.
8. B. R. Tittmann and L. Ahlberg, "Measurements of scattering from
   bulk defects", in Proceedings of the DARPA AFML Review of Progress
   in Quantitative NDE AFWAL-TR-81-4080 (Air Force Wright Aeronau-
   tical Laboratories, Dayton, 1980), pp. 311-319.
9. See, for example, J. D. Achenbach, A. K. Gauteson and H. McMaken,
   Ray methods for waves in elastic solids with applications to scat-
   tering from cracks (Pittman, London, 1982).
10. W. Kohn and J. R. Rice, "Scattering of long-wavelength elastic
    waves from localized defects in solids", J. Appl. Phys. $\underline{50}$, 3353
    (1979).
11. J. M. Richardson, "The inverse problem in elastic wave scattering
    at long wavelength", 1978 Ultrasonic Symposium Proceedings (IEEE,
    New York, 1978), pp. 759-766.
12. A. K. Mal and L. Knopoff, "Elastic wave scattering in two compo-
    nent systems", J. Inst. Math. Appl. $\underline{3}$, 376-387 (1967).
13. J. E. Gubernatis, E. Domany and J. A. Krumhansl, "Formal aspects
    of the scattering of ultrasound by flaws in elastic materials",
    J. Appl. Phys. $\underline{48}$, 2804-2811 (1977).
14. Handbook on Acoustic, Electromagnetic and Elastic Wave Scatter-
    ing, Vols. 1 & 2, V. K. Varadan and V. V. Varadan, Eds., (North
    Holland, Amsterdam, in press).
15. W. M. Visscher, "Calculation of the scattering of elastic waves
    from a penny-shaped crack by the method of optimal truncation",
    Wave Motion $\underline{3}$, 49 (1981).

16. W. M. Visscher, "A new way to calculate scattering of acoustic and elastic waves. I. Theory illustrated for scalar waves", J. Appl. Phys. 51, 825 (1980).

17. V. Varatharajulu (V. V. Varadan) and Y. H. Pao, "Scattering matrix for elastic waves. I. Theory", J. Acoust. Soc. Am. 60, 556 (1976).

18. V. V. Varadan, "Scattering matrix for elastic waves. II. Application to elliptic cylinders", J. Acoust. Soc. Am. 1014 (1978).

19. J. L. Opsal, "Calculations of elastic wave scattering from voids and crack-like defects by the method of optimal truncation". Proceedings of the DARPA AFML Review of Progress in Quantitative NDE, report AFWAL-TR-81-4080 (Air Force Wright Aeronautical Laboratories, Dayton, 1980), pp. 292-299.

20. N. Bleistein and J. K. Cohen, "Progress on a mathematical inversion technique for nondestructive evaluation", Wave Motion 2, 75 (1980).

21. J. D. Achenbach, K. Viswanathan and A. Norris, "An inversion integral for crack scattering data", Wave Motion 1, 299 (1979).

22. J. D. Achenbach, A. N. Norris, L. A. Ahlberg and B. R. Tittmann, "Crack mapping by ray methods", in reference 6.

23. J. H. Rose and J. A. Krumhansl, "Determination of flaw characteristics from ultrasonic scattering data", J. Appl. Phys. 50, 2951 (1979).

24. J. M. Richardson, "The deterministic problem in the scattering of elastic waves from weak inhomogenities", in, Ultrasonics Symposium Proceedings, Eds., J. deKlerk and B. R. McAvoy, pp. 356-360 (1979).

25. D. A. Lee, Modeling and simulation, 12, 1253 (1982).

26. J. H. Rose and J. M. Richardson, "Time domain Born approximation", J. Nondestructive Evaluation, 3, 45 (1982).

27. J. H. Rose and J. L. Opsal, "The inverse Born approximation: An exact procedure for determining flaw shape", in ref. 6.

28. K. M. Lakin and A. R. Landin, "Acoustic imaging with two-dimensional arrays", in Ref. 5, pp. 777-790.

29. D. K. Peterson, R. Baer, K. Liang, S. D. Bennett, B. T. Khuri-Yakub and G. S. Kino, "Quantitative evaluation of real-time synthetic aperture acoustic images", in Ref. 5, pp. 767-776.

30. R. B. Thompson, K. M. Lakin and J. H. Rose, "A comparison of the inverse Born and imaging techniques for flaw reconstruction", 1981 Ultrasonics Symposium Proceedings, pp. 930-935.

31. R. K. Elsley and R. C. Addison, "Dependence of the accuracy of the Born inversion on noise and bandwidth", in, Proceedings of the DARPA AFML Review of Progress in Quantitative NDE, report AFWAL-TR-81-4080 (Air Force Wright Aeronautical Laboratories, Dayton, 1980), pp. 389-393.

32. D. K. Hsu, J. H. Rose and D. O. Thompson, "Quantitative experimental characterization of inclusions in solids by the inverse Born algorithm", in Ref. 6.

33. J. H. Rose and J. L. Opsal, "Inversion of ultrasonic data", in Ref. 5, pp. 187-195.

34. T. A. Gray and R. B. Thompson, "Ultrasonic flaw detection in turbine rotor components", in Ref. 6.

35. R. C. Addison, Jr., R. K. Elsley and L. J. Graham, "Flaw detection below curved surfaces of components", in Ref. 6.

36. R. B. Thompson and T. A. Gray, "A model relating ultrasonic scattering amplitudes to measurements through liquid solid interfaces", J. Acoust. Soc. Am., 74, 1279 (1983).

37. W.-M Boerner, "Polarization utilization in electromagnetic inverse scattering" in Inverse Scattering Problems in Optics, Ed., H. P. Baltes (Springer-Verlag), 1980.

38. J. H. Rose, "Exterior reconstruction of a three dimensional scatterer", Wave Motion, 6, 149 (1984).

39. J. M. Richardson, "The theory of flaw centroids and low frequency phase shifts - a review", in Ref. 5, pp. 197-202.

40. J. M. Richardson, "Scattering of elastic waves from symmetric inhomogeneities at low frequencies", Wave Motion, 6, 325 (1984).

41. C. F. Ying and R. Truell, "Scattering of a plane longitudinal wave by a spherical obstacle in an isotropically elastic solid", J. Appl. Phys. 27, 1086 (1956).

42. R. K. Elsley and J. H. Rose, unpublished.

43. J. H. Rose and J. A. Krumhansl, "A technique for determining flaw characteristics from ultrasonic scattering amplitudes", in, The Fourth Annual Report, DARPA/AFML Interdisciplinary Program for Quantitative Flaw Definition (Air Force Materials Laboratory, Wright-Patterson AFB, Dayton, OH 45433), pp. 1,5.

44. D. K. Hsu, J. H. Rose, R. B. Thompson and D. O. Thompson, "Quantitative characterization of flaws near a surface using the inverse Born approximation", J. Nondestructive Evaluation, 3, 183 (1982).

45. J. H. Rose, V. V. Varadan, V. K. Varadan, R. K. Elsley and B. R. Tittmann, "Inversion of ultrasonic scattering data", in, Acoustic, Electromagnetic and Elastic Wave Scattering - Focus on the T-Matrix Approach, V. K. Varadan and V. V. Varadan, Eds., (Pergamon Press, New York (1980), pp. 605-614.

46. R. K. Elsley, "Inversion algorithms for crack-like flaws", in, Ref. 5, pp. 537-545.

47. J. H. Rose, J. L. Opsal, F. Cohen-Tenoudji and B. R. Tittmann, unpublished.